SEDIMENTOLOGY the journal of the International Association of Sedimentologists

Sedimentology (2010) doi: 10.1111/j.1365-3091.2010.01168.x

Turbidite system architecture and sedimentary processes along topographically complex slopes: the Makran convergent margin

JULIEN BOURGET*,[1], SEBASTIEN ZARAGOSI*, NADINE ELLOUZ-ZIMMERMANN†, NICOLAS MOUCHOT‡, THIERRY GARLAN§, JEAN-LUC SCHNEIDER*, VALENTINE LANFUMEY¶ and SIGFRIED LALLEMANT‡

**Université de Bordeaux, UMR CNRS 5805 EPOC, Avenue des Facultés, F-33405 Talence, France (E-mail: julien.bourget@gmail.com)*

†IFP, Geology-Geochemistry-Geophysics, 1 & 4 avenue de Bois Préau, F-92852 Rueil-Malmaison, France

‡Université de Cergy-Pontoise, GEC, 5, mail Gay-Lussac, F-95031 Cergy-Pontoise, France

§SHOM, Centre Hydrographie, BP 426, F-29275 Brest, France

¶IFREMER, GM/LES, BP70, F-29280 Plouzané Cedex, France

Associate Editor – Subhasish Dey

ABSTRACT

This study investigates the morphology and Late Quaternary sediment distribution of the Makran turbidite system (Makran subduction zone, north-west Indian Ocean) from a nearly complete subsurface mapping of the Oman basin, two-dimensional seismic and a large set of coring data in order to characterize turbidite system architecture across an active (fold and thrust belt) margin. The Makran turbidite system is composed of a dense network of canyons, which cut into high relief accreted ridges and intra-slope piggyback basins, forming at some locations connected and variably tortuous paths down complex slopes. Turbidite activity and trench filling rates are high even during the Holocene sea-level highstand conditions. In particular, basin-wide, sheet-like thick mud turbidites, probably related to major mass wasting events of low recurrence time, drape the flat and unchannellized Oman abyssal plain. Longitudinal depth profiles show that the Makran canyons are highly disrupted by numerous thrust-related large-scale knickpoints (with gradients up to 20° and walls up to 500 m high). At the deformation front, the strong break of slope can lead to the formation of canyon-mouth 'plunge pools' of variable shapes and sizes. The plunge pools observed in the western Makran are considerably larger than those previously described in sub-surface successions; the first insights into their internal architecture and sedimentary processes are presented here. Large plunge pools in the western Makran are associated with large scoured areas at the slope break and enhanced sediment deposition downstream: high-amplitude reflectors are observed inside the plunge pools, while their flanks are composed of thin-bedded, fine-grained turbidites deposited by the uppermost part of the turbidity flows. Thus, these architectural elements are associated with strong sediment segregation leading to specific trench-fill mechanisms, as only the finer-grained component of the flows is transferred to the abyssal plain. However, the Makran accretionary prism is characterized by strong along-strike variability in tectonics and fluvial input distribution that might directly influence the turbidite system architecture (i.e. canyon entrenchment, plunge pool formation or channel development at canyon mouths), the sedimentary

[1]Present address: Australian School of Petroleum, Reservoir Analogue Research Group, University of Adelaide, SA 5005, Australia.

dynamics and the resulting sediment distribution. Channel formation in the abyssal plain and trench-fill characteristics depend on the theoretical 'equilibrium' conditions of the feeder system, which is related closely to the balance between erosion rates and tectonic regime. Thus, the Makran turbidite system constitutes an excellent modern analogue for deep-water sedimentary systems with structurally complex depocentres, in convergent margin settings.

Keywords Active margin, gravity flow, Gulf of Oman, hydraulic jump, plunge pool, slope break deposits, submarine slope, turbidite system.

INTRODUCTION

Early conceptual models of turbidity current deposition and submarine turbidite system development essentially envisaged the development of channel-levée systems associated with unconfined, fan-shaped distal sediment bodies. However, a wealth of case studies from several recent and ancient turbidite systems worldwide makes it clear that sediment distribution and geometries of depositional bodies vary significantly within systems located on topographically complex slopes (e.g. Kneller & McCaffrey, 1999; Prather, 2000; Sinclair & Tomasso, 2002; Prather, 2003; Lomas & Joseph, 2004; Smith, 2004). Reservoir models derived from Neogene Gulf of Mexico salt-withdrawal basins (e.g. Prather *et al.*, 1998; Beaubouef & Friedman, 2000) are usually cited in studies of structurally complex slope depocentres. However, there is significant variation in the characteristics of tectonic deformation and submarine slope topography between Gulf of Mexico intra-slope basins and thrust-belt controlled slopes as developed in accretionary prism settings (e.g. Covault *et al.*, 2009), that may lead to both different sediment distribution and turbidite system architecture. Smith (2004) proposed that sediment distribution systems on topographically complex slopes can consist of *cascades of silled basin* (or disconnected, intraslope basins, such as the Gulf of Mexico slope with salt-withdrawal-created mini basins) and a *connected tortuous corridor* [defined as a laterally confined depression (or a canyon) evolving on a topographically complex slope, that can connect several intra-slope basins]. Fold and thrust-belt controlled submarine slopes of accretionary prisms, which usually show several partially silled basins with lateral escape paths, lie within the latter one. However, continental slope morphology and downslope sediment transport along accretionary prisms are often complex, and primarily depend on the balance between deformation rates (uplift of slope ridges) and erosion rates by submarine canyons (e.g. Underwood & Karig, 1980; Huyghe *et al.*, 2004). In addition, due to the lack of data in modern analogues of tectonically controlled systems, it remains unclear whether 'classical' architectural elements of turbidite systems, as defined by Payton (1977) or Mutti & Normark (1991), among others, are observed or not, and how their geometries can differ from passive-margin fan architectural elements. As an example, the importance of tectonically induced break of slopes has been evidenced by the occurrence of abrupt canyon terminations in abyssal plains (for example, submarine 'plunge pools' of Farre & Ryan, 1985; Lee *et al.*, 2002). Such atypical architectural elements are poorly documented, and the sedimentary processes related to them are still unknown. In accretionary prisms, strong breaks of slope are observed classically at the deformation front, corresponding to the continental slope/abyssal plain transition. However, how does uplift of accretionary ridges at the deformation front impact the sedimentary processes and the geometry of sedimentary bodies? Does it control the mechanisms of sediment transfer and transport in the trenches?

These questions have been investigated in the Oman basin, for which the present data cover 166 700 km^2. This basin offers an excellent opportunity to investigate the sediment dispersal patterns and their architectural elements in the context of convergent margins. The Makran accretionary prism exhibits: (i) high convergence rates of about 2·5 to 4 cm $year^{-1}$ (Ellouz-Zimmermann *et al.*, 2007a) resulting in highly deformed sea floor, composed of intra-slope (piggyback) basins and accreted ridges; and (ii) significant continental erosion by numerous ephemeral streams located in an arid environment controlled by the Asian monsoon climate, that supports high rates of sediment transfer to the deep sea (von Rad *et al.*, 1999a). The large data set available on this system (multibeam echo sounder data, sedimentary cores and seismic lines acquired during the MARABIE and CHAMAK surveys) has been

analysed in order to address: (i) the overall morphology of the present-day turbidite system and its architecture; (ii) the sediment dispersal pattern and the role of pre-existing sea floor topography on the gravity current deposition at the deformation front (i.e. continental slope to abyssal plain transition) and downstream; and (iii) the along-strike relationships between the margin-scale tectonic regime, the fluvial input and the architecture of the Makran turbidite system at both the system and architectural element scales.

REGIONAL SETTING

Geodynamic setting

The Makran accretionary prism results from the northward subduction of the Arabian Sea beneath the Iranian and Afghan continental blocks, now accreted to the Eurasian continent (Fig. 1). Subduction started during Late Cretaceous times and continued fairly continuously until present times (Kukowski *et al.*, 2001; Ellouz-Zimmermann *et al.*, 2007a; Grando & McClay, 2007). The western part of the Arabian Sea lithosphere belongs to the Arabian plate, whereas the eastern part belongs to the Indian plate; their present-day plate boundary runs along the dextral transform Owen Fracture Zone (Gordon & Demets, 1989; Fournier *et al.*, 2001). The plate boundary shows a nearly east–west bend along the Murray Ridge before intersecting the subduction boundary west of Karachi City (Ellouz-Zimmermann *et al.*, 2007b; Fig. 1). The actual plate convergence rate has been estimated at 4 cm year^{-1} using classical plate modelling (DeMets *et al.*, 1994), whereas recent space geodesy modelling and a GPS-based model estimated the present-day velocities between 2·5 cm year^{-1} in the western Makran area and 3 cm year^{-1} in the eastern Makran area (Ellouz-Zimmermann *et al.*, 2007b; Grando & McClay, 2007).

The Makran subduction zone is considered as an area of important earthquake activity, and is a part of the two main tsunamigenic zones in the Indian Ocean (Heidarzadeh *et al.*, 2009). The

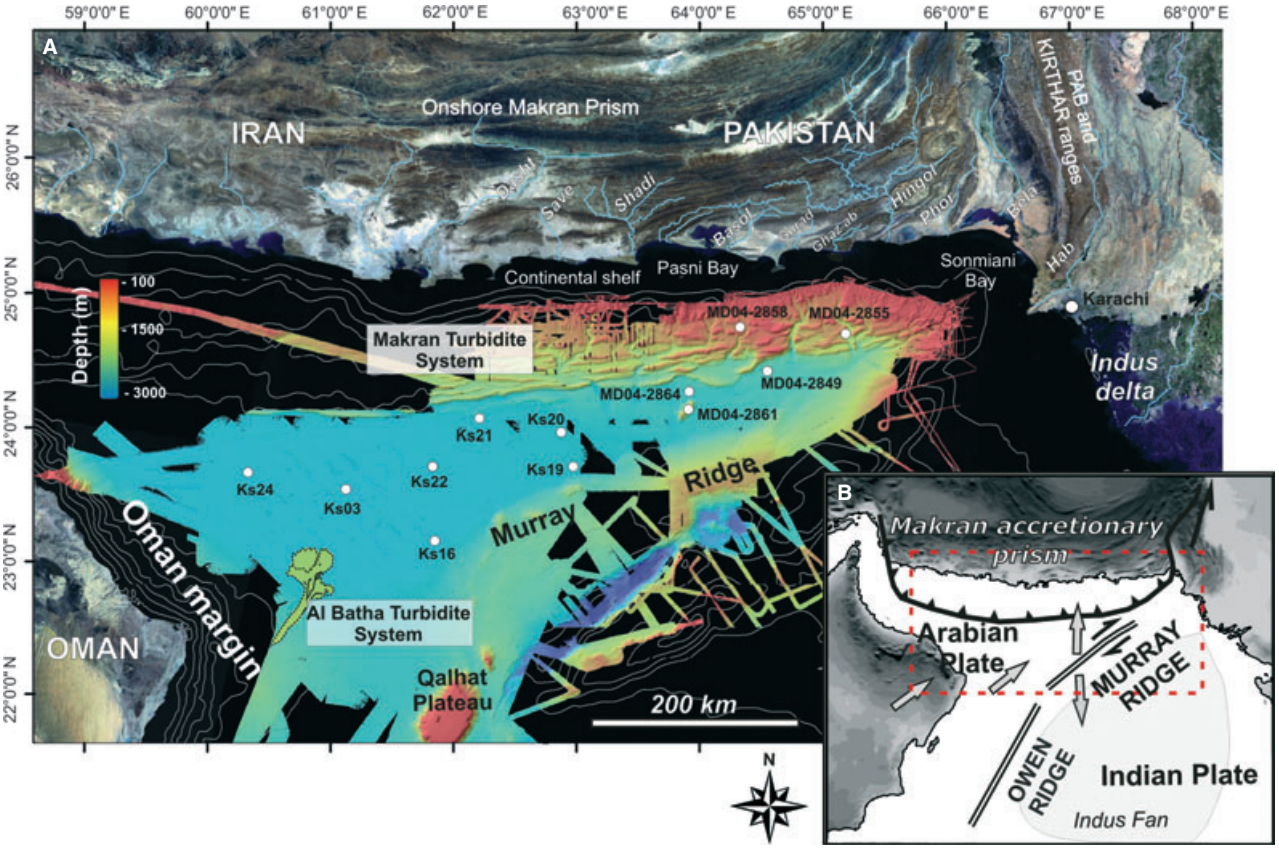

Fig. 1. (A) Location map and physiography of the study area. Compilation of multibeam bathymetry in the Gulf of Oman from the MARABIE (SHOM) and CHAMAK (IFP) cruises, combined with the existing hydrosweep data (Flueh *et al.*, 1997). White dots indicate the location of sedimentary cores used in this study. (B) Tectonic setting (simplified) of the Gulf of Oman.

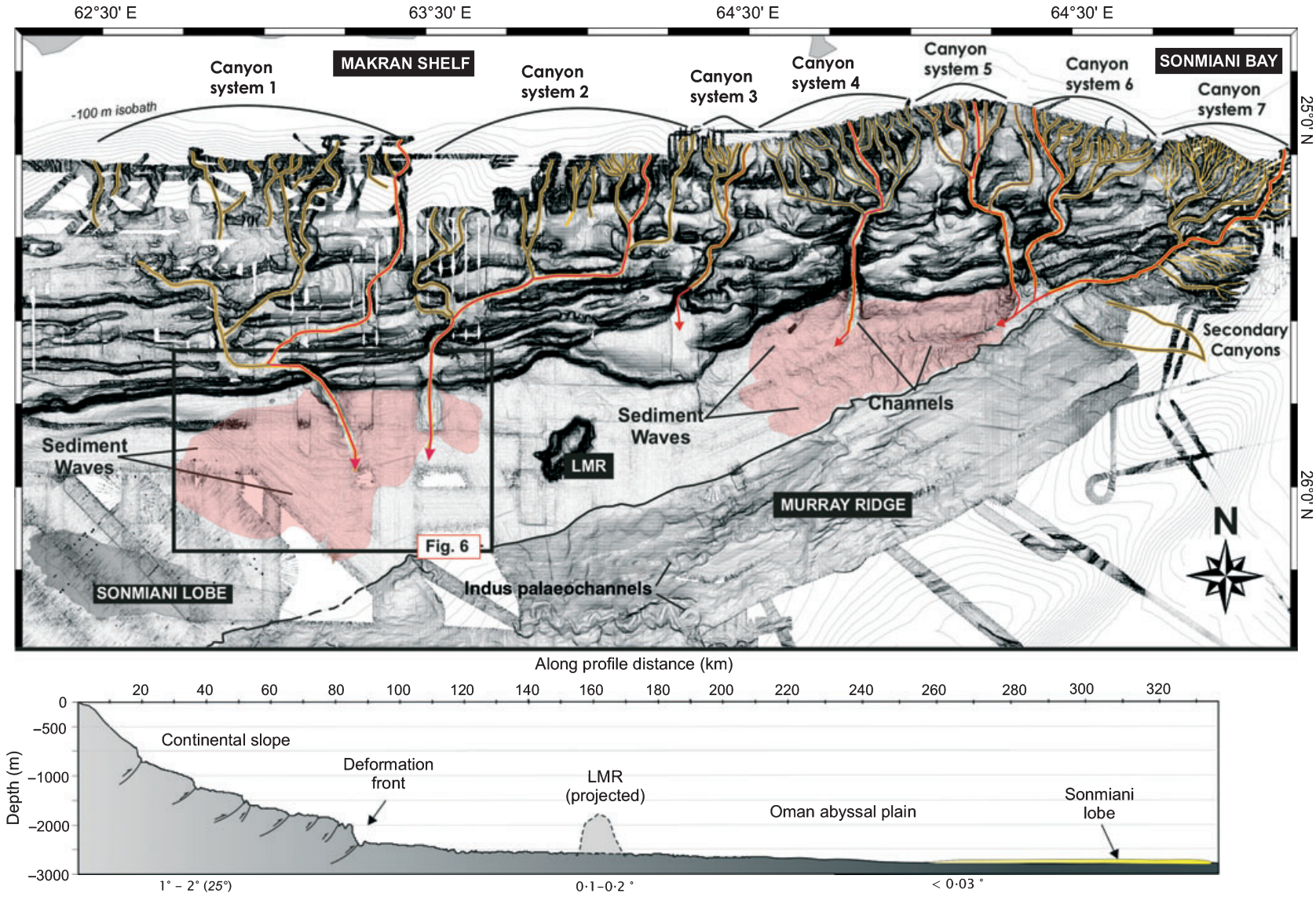

Fig. 2. Slope map of the Makran turbidite system, showing the seven canyon systems (yellow), their main pathway (red) and the main architectural elements in the abyssal plain. Longitudinal depth profiles of these canyon pathways are shown in Fig. 4. The cross-section (below) shows a general longitudinal profile of the Makran margin from the upper slope (Canyon 5) to the Oman abyssal plain, with main slope changes.

1945 Makran earthquake (M_w = 8·1 to 8·3), the largest earthquake known in this region, triggered a destructive tsunami related to both coastal uplift (with eruption of mud volcanoes) and submarine landslides (Ambraseys & Melville, 1982; Byrne *et al.*, 1992). During this event, submarine Makran telegraph cables were also severed at eight places offshore, suggesting that gravity current(s) were initiated by the landslide(s).

The Makran accretionary prism is more than 350 km wide (Platt *et al.*, 1985). Over 60% of the prism is presently sub-aerial (Ellouz-Zimmermann *et al.*, 2007b) and only the frontal 100 to 150 km are submarine (Kukowski *et al.*, 2001; Figs 1 and 2). The transition between the emerged part of the Makran and the offshore compression front is expressed by a nearly undeformed platform (Ellouz-Zimmermann *et al.*, 2007a). The continental shelf is relatively narrow (from 10 to 40 km wide), with a shelf break at 30 to 50 m water depth that extends to *ca* 100 m off the Sonmiani Bay. The offshore prism consists of a sequence of thrust slice units forming accretionary ridges (Fig. 2) with steep flanks and variable length, associated with intraslope 'piggyback' basins (White & Louden, 1983; Fruehn *et al.*, 1997; Kukowski *et al.*, 2001; Ellouz-Zimmermann *et al.*, 2007b; Grando & McClay, 2007).

From the western part to the eastern part of the offshore prism, the average slope gradient increases, the bathymetry profile shallows, and the size, length and distance between each thrust decrease dramatically (Ellouz-Zimmermann *et al.*, 2007b). The abyssal plain (3200 m water depth) forms a smooth trench with low gradients, and is confined southward by the Murray Ridge (Fig. 1). The abyssal plain deepens and widens gently to the west towards the centre of the Oman basin (Fig. 1), where it becomes unconfined. It is disturbed locally by more or less buried south-west to north-east trending bathymetric highs (Kukowski *et al.*, 2001; Ellouz-Zimmermann *et al.*, 2007b), such as the Little Murray Ridge (LMR; Fig. 2).

Regional climate

The north-eastern Arabian Sea climate is dominated by the seasonal reversal of the monsoon winds (Sirocko *et al.*, 1991; von Rad *et al.*, 1995; Luckge *et al.*, 2001; Clemens & Prell, 2003) that leads to a marked seasonal productivity and sediment input variability (von Rad *et al.*, 1999a; Sirocko *et al.*, 2000; Reichart *et al.*, 2002). Summer monsoon moist winds blow from the south-west and lead to warm and humid conditions and a precipitation maximum over Karachi and the Indian subcontinent (Luckge *et al.*, 2001), whereas arid to semi-arid conditions generally dominate during the winter monsoon. However, the Makran area corresponds to the present-day northern limit summer position of the Intertropical Convergence Zone (Gasse, 2000; Fleitmann *et al.*, 2007). At present, it shows a maximum precipitation during the winter monsoon when cyclonic low-pressure systems originating in the Eastern Mediterranean occasionally penetrate the Arabian landmass (Weyhenmeyer *et al.*, 2000; Luckge *et al.*, 2001). Hence, winter corresponds to the present-day maximum sediment input from the numerous ephemeral streams and rivers located along the Makran coast (Luckge *et al.*, 2001). The strong seasonality causes intense (flash) flooding of the drainage system, and precipitation is the main factor influencing terrigenous input along the margin in the semi-arid Makran coastal area (Prins *et al.*, 1999; von Rad *et al.*, 1999a). Very high sediment transfer rates from the desert Makran streams is also favoured by the tectonic uplift on the Makran hinterland (from mm $year^{-1}$ to cm $year^{-1}$; Page *et al.*, 1979) that lead to rapid rejuvenation of the drainage system and enhanced erosion of the onshore Makran deposits (Snead, 1967; von Rad *et al.*, 1999a).

THE MAKRAN TURBIDITE SYSTEM

Sediment input history within the Makran prism growth can be divided into two stages (Ellouz-Zimmermann *et al.*, 2007b). The initial stage of sediment input up to Miocene times corresponds to the early stages of the collision zone, which is coupled with the deposition and progressive accretion of the Himalayan turbidites (Stoffers & Ross, 1979; Kukowski *et al.*, 2001; Grando & McClay, 2007) through the shortening of a palaeo-Indus deep-sea fan more or less parallel to the palaeo-trench. After the Late Miocene and the southward migration of the palaeo-Indus delta and deep-sea fan, the accretionary complex mostly recycles sediments coming from the erosion of the onshore prism itself, through a series of river and canyon systems (Ellouz-Zimmermann *et al.*, 2007a,b). Since the Plio-Pleistocene, most of the Himalaya-derived sediments have been trapped in the Indus fan (Prins & Postma, 2000) and only the sediments derived from the

onshore Makran area are involved in the turbidite system growth (Mouchot *et al.*, in press).

The present-day Makran turbidite system has been mapped along a width of 500 km and shows a mean length of 80 km (Fig. 1). Ellouz-Zimmermann *et al.* (2007b) and Mouchot *et al.* (in press) showed that it is composed of several canyons which cross along the accreted ridges and piggyback basins. While canyons are characterized by a high-backscatter facies, piggyback basins generally show a low to very low reflectivity at 13 kHz, suggesting fine-grained sedimentation (Mouchot *et al.*, in press). Cores from Prins *et al.* (1999) and Stow *et al.* (2002) in the western prism showed that turbidite sedimentation has been active during the Late Quaternary and during the Holocene rising sea-level.

DATA SET AND METHODS

Multibeam bathymetry and acoustic imagery were collected using the multibeam echo sounder SIMRAD EM12 (13 kHz) and EM300 (30 kHz; Kongsberg Maritime AS, Horten, Norway). and SeaFalcon 12 kHz (Thales UnderWater Systems, Stockport, UK) during the survey MARABIE 2000 (*R/V Atalante*, IFREMER), MARABIE 2001 (*R/V Le Suroît*, IFREMER), and CHAMAK 2004 (*R/V Marion-Dufresne*, IPEV), respectively. These data were combined with the existing hydrosweep bathymetry from the cruise SO 123 'MAMUT' of *R/V Sonne* 1997 (Flueh *et al.*, 1997), resulting in a nearly complete mapping of the Makran continental slope and abyssal plain (Fig. 2).

Sub-bottom seismic lines (3·5 kHz) were collected during the MARABIE and CHAMAK cruises (Mouchot *et al.*, in press). In addition, around 1000 km of multichannel seismic lines have been acquired during the CHAMAK survey. The seismic sources were produced by an array of four sleeve guns (total volume of about 110 inch^3) and recorded by two short streamers (respectively, a 100 m long six-channel streamer and a 180 m long 18 channel streamer) allowing investigation of the sediments down to 2·5 sec [two-way time (TWT)] with a relatively high spatial resolution.

Twenty-four Kullenberg piston cores were collected in the abyssal plain during the MARABIE 2001 survey, and 13 long (Calypso) piston cores were collected in different sectors of the prism during the CHAMAK survey (Ellouz-Zimmermann *et al.*, 2007b). The key characteristics of the 12 cores used in this study are displayed in Table 1. For each core, thin slabs (15 mm thick) were sampled and analysed in the SCOPIX X-ray image processing tool (Migeon *et al.*, 1999). Grain-size analyses were performed using a Malvern™ Supersizer 'S' (Malvern Instruments Limited, Malvern, Worcestershire, UK). This approach allowed a very detailed analysis of sedimentary structures and turbidite/hemipelagite–pelagite distinction. Observations of thin sections (10 to 25 cm long) of indurated sediments selected from well-preserved sedimentary facies were performed using a fully automated Leica™ DM6000B Digital Microscope (Leica Microsystems Inc., Wetzlar, Germany) (Zaragosi *et al.*, 2006). Finally, semi-quantitative geochemical analyses were performed on the cores KS24, MD04-2849, MD04-2855 and MD0428-58 using the Avaatech© XRF 'Core scanner' (Avaatech, Den Burg, The Netherlands) at centimetre to millimetre scale. Additional carbonate content measurements (on the cores KS16, KS03 and KS15) were performed using gasometrical calcimetry. Core stratigraphy has

Table 1. Key characteristics of the 12 cores used in this study.

Core no.	Core location (latitude, longitude)	Depositional environment	Depth (m b.s.l.)	Length (m)
MD04-2858	65°10′48·459′ E, 24°42′13·138′ N	Upper slope piggyback basin	1515	25·5
MD04-2855	64°19′42·429′ E, 24°44′55·814′ N	Mid-slope piggyback (Canyon 5 flank)	1845	22
MD04-2849	64°33′14·469′ E, 24°25′39·251′ N	Canyon 4 mouth	3037	34
MD04-2864	63°55′0·230′ E, 24°15′34·479′ N	Eastern abyssal plain (base of slope)	3165	35
KS 20	62°52′19·891′ E, 23°57′27·367′ N	Canyon 1 sediment waves	3277	9
KS 21	62°12′55·214′ E, 24°3′55·589′ N	Canyon 1 sediment waves	3351	9·4
KS 19	62°58′32·202′ E, 23°42′48·036′ N	Sonmiani Lobe	3282	5·1
KS 24	60°19′53·120′ E, 23°39′51·969′ N	Western abyssal plain	3362	9·4
KS 22	61°49′46·596′ E, 23°42′38·771′ N	Central abyssal plain	3348	9·3
KS 03	61°7′50·982′ E, 23°32′36·149′ N	Central abyssal plain	3357	13·1
KS 16	61°50′46·970′ E, 23°9′13·222′ N	Central abyssal plain	3365	9·8
MD04-2861	63°54′53·186′ E, 24°7′55·751′ N	Little Murray Ridge	2093	31

Table 2. Radiocarbon ages of cores used in this study.

Core no.	Depth in core (cm)	Material	Uncorrected ^{14}C age (cal kyr BP)	Calendar age (cal yr BP)
MD04-2849	550 to 560	Bulk planktonic foraminifera	3215 ± 30	3027
MD04-2849	1142 to 1144	Bulk planktonic foraminifera	7250 ± 30	7711
MD04-2849	1475 to 1476	Bulk planktonic foraminifera	9270 ± 45	10 116
MD04-2849	1835 to 1836	Bulk planktonic foraminifera	13 270 ± 60	15 191
MD04-2849	2032 to 2035	Bulk planktonic foraminifera	13 870 ± 40	16 005
MD04-2849	2866 to 2867	Bulk planktonic foraminifera	15 630 ± 60	18 644
MD04-2849	3376 to 3377	Bulk planktonic foraminifera	18 580 ± 90	21 629
MD04-2855	1030 to 1031	Bulk planktonic foraminifera	13 400 ± 60	15 146
MD04-2855	2241 to 2245	Bulk planktonic foraminifera	47 700 ± 1200	50 252
MD04-2861	339 to 340	Bulk planktonic foraminifera	14 160 ± 60	16 385
MD04-2864	678 to 683	Bulk planktonic foraminifera	8390 ± 35	8992
MD04-2864	1575 to 1577	Bulk planktonic foraminifera	15 065 ± 45	17 759
KS03	340 to 342	Bulk planktonic foraminifera	2140 ± 30	1733
KS03	530 to 533	Bulk planktonic foraminifera	3030 ± 30	2795
KS03	1045 to 1047	Bulk planktonic foraminifera	3290 ± 30	3136
KS16	315 to 316	Bulk planktonic foraminifera	2390 ± 30	2020
KS20	217 to 218	Bulk planktonic foraminifera	4465 ± 35	4656
KS20	482 to 483	Bulk planktonic foraminifera	5865 ± 40	6283
KS20	660 to 661	Bulk planktonic foraminifera	6415 ± 30	6896
KS20	717 to 718	Bulk planktonic foraminifera	6775 ± 30	7304
KS20	871 to 872	Bulk planktonic foraminifera	8295 ± 30	9573
KS21	197 to 199	Bulk planktonic foraminifera	4730 ± 30	4958
KS21	278 to 279	Bulk planktonic foraminifera	5630 ± 30	6029
KS21	355 to 356	G. Ruber + G. Trilobus	6445 ± 30	6933
KS21	460·5 to 461·5	Bulk planktonic foraminifera	7605 ± 35	8065
KS21	618 to 619	Bulk planktonic foraminifera	9715 ± 35	10 568
KS21	794·2 to 796	N. Dutertrei	12 160 ± 60	13 613
KS21	880·5 to 882	N. Dutertrei	13 065 ± 50	14 942

been completed using ^{14}C AMS dating from bulk or single species planktonic foraminifera (Table 2) sampled in hemipelagic/pelagic intervals. Radiocarbon dates have been corrected for a marine reservoir effect of 408 years and calibrated to calendar years using CALIB Rev 5.0/Marine04 data set (Stuiver *et al.*, 2005) up to 21·78 ^{14}C ka and Bard (1998) thereafter. Radiocarbon ages of this study were performed at the 'Laboratoire de Mesure du Carbone 14' in Saclay ('SacA').

ARCHITECTURE OF THE MAKRAN TURBIDITE SYSTEM

The continental slope

Submarine canyons

The Makran continental slope is cut by a dense dendritic canyon network (Fig. 2) which is located directly off the network of small ephemeral streams (wadis) and a few major, but seasonal, rivers such as the Hingol, Phor and Hab Rivers (Fig. 1, Table 3). Canyons and gullies are grouped into seven major submarine drainage systems that finally form seven outlets in the lower slope (i.e. Canyons 1 to 7; Fig. 2). The main characteristics of each canyon system are given in Table 3. The longitudinal thalweg profile and slope gradient have been plotted for each of the Makran canyons (restricted to the most developed contributor for each canyon system). Generally, the profiles can be divided into two segments: the first segment corresponds to the Makran slope where the thalweg profile is clearly disturbed by thrust faulting along accretionary ridges. This effect is seen clearly in the case of Canyon 5, where seven major knickpoints are observed and can easily be correlated with the seven accreted ridges (Fig. 3). The second segment corresponds to the abyssal plain and is characterized by gentle gradients and a smooth profile (Figs 2 and 3). In the present study, a knickpoint is defined as a disruption in the equilibrium profile (Gardner, 1983; Heiniö & Davies, 2007). Both the morphology of the canyons and the shape of their depth profile vary along strike (Figs 2 and 4).

In the western prism, extended (>150 km long), sinuous canyons develop (Canyon systems 1 and

Table 3. Main morphological parameters of the Makran canyon systems.

	Canyon system 1	Canyon system 2	Canyon sytstem 3	Canyon system 4	Canyon system 5	Canyon system 6	Canyon system 7
Main rivers	Save	Shadi, Basol	Basol	Gurad	Ghaz Ab	Hingol	Phor, Porali, Hab
Total length (km)	161	152	83	82	90	85	115
Direction	Cross-strike	Cross-strike	Cross-strike	Cross-strike	Cross-strike	Cross-strike	Along strike
Drainage system width (upper slope) (km)	102	82	19	50	31	48	98
Sinuosity	0·62	0·82	0·87	0·94	0·9	0·85	0·87
Piggyback basins connections	Yes	Yes	No	No	No	No	Yes
Longitudinal depth profile	Highly disrupted	Highly disrupted	Highly disrupted	Disrupted below 2300 m	Disrupted	Poorly disrupted	Very poorly disrupted
Knickpoint at deformation front	4 km long, 625 m high	4 km long, 400 m high	–	1 km long, 300 m high	2 km long, 415 m high, 1·6 km/100 m	1·5 km long, 180 m high	<1 km long, <100 m high
Plunge pools [length (km)/depth (m)]	20/300	15/150	–	2 to 2·5/<150	–	1·8/120	None
Channel development	No/breach in the rampart	None	None	Little	–	Yes	–
Maximum channel size [width (km)/depth (m)]	–	–	–	6/70	–	8/150	–
Sediment waves height (minimum to maximum) (m)	<5 to 25	2 to 15	–	11 to 39	–	14 to 57·5	–
Sediment waves λ (minimum to maximum) (km)	0·6 to 4·5	0·6 to 3	–	1·5 to 5·4	–	3·9 to 4·7	–
Sediment waves echo-facies	Echo-facies Ia	Echo-facies Ia	–	?	–	Echo-facies Ib/Iia*	–
Holocene turbidite sedimentation rates	–	–	–	–	–	–	–

*From Mouchot *et al.* (2010).

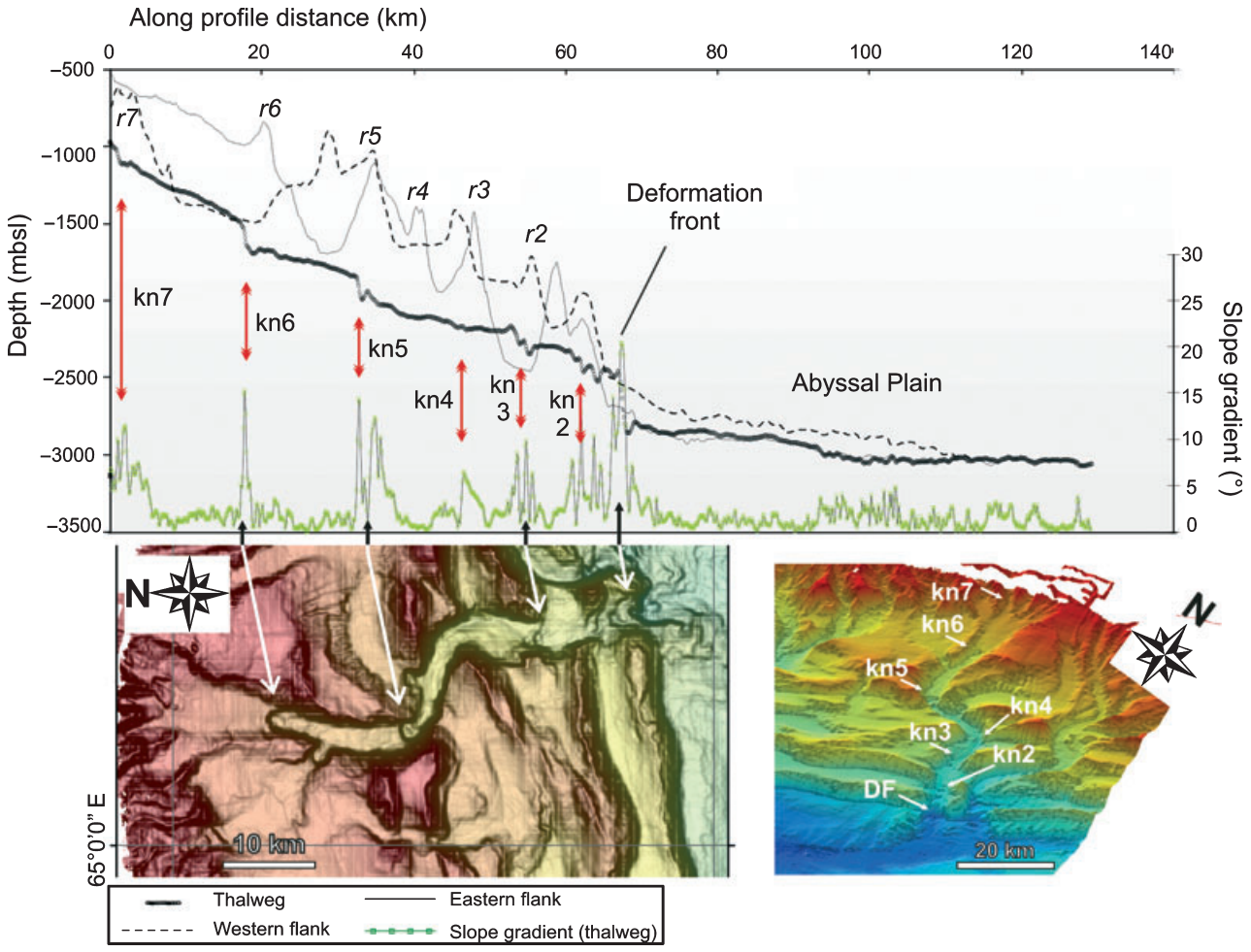

Fig. 3. Longitudinal depth profile [metres below sea-level (m b.s.l.)] and slope gradient (absolute values, in degrees) of Canyon 5, with locations of the main knickpoints shown. Identification of the knickpoints on the shaded bathymetry of the Canyon 5 in plan view (left) and 3D (right). Location of profile is shown in Fig. 2.

2); they connect and follow some of the piggyback basins, with changes in direction when encountering the accretionary ridges (Fig. 2). Canyon 3 is disconnected from the abyssal plain (Fig. 2) and terminates in a wide, flat piggyback basin at the deformation front. The western canyons are associated with very disrupted longitudinal depth profiles, with major knickpoints observed when the canyons reach the deformation front (Fig. 4); their profiles are only smoothed where the canyon pathways follow piggyback basins (Fig. 4).

In the eastern prism, canyon morphology evolves towards shorter systems (<90 km long), mostly rectilinear (for example, Canyon systems 4 to 6) and disconnected from the piggyback basins (Fig. 2). The thalweg profile of Canyon 4 displays a concave-up, poorly disrupted profile until *ca* 2200 m water depth, and major irregularities and a convex-up shape are observed close to the anticlines of the first and second accreted ridges (Fig. 4). Eastward, the thalweg profiles along the canyons are also disrupted by knickpoints, but the profiles progressively smooth (Fig. 4). Canyon system 7, which develops offshore from Sonmiani Bay, is the only one to trend along strike (i.e. parallel to the accreted ridges; Fig. 2). It shows a globally concave-up thalweg profile, near to a theoretical equilibrium profile (Fig. 4).

Plunge pools and canyon-mouth architecture

Marked topographic depressions are observed at the mouths of Canyons 1 and 2 in the western prism (labelled P1 and P2, respectively; Fig. 5 and Table 3). These depressions correspond to canyon-mouth submarine plunge pools (*sensu* Farre & Ryan, 1985; Lee *et al.*, 2002). P1 is 20 km long, reaches a maximum of 300 m deep and 8 km wide, while P2 is 15 km long, reaches 150 m deep and 7 km wide (Fig. 5). Internal thalweg or scours (1 to 1·7 km wide, 4 to 8 km

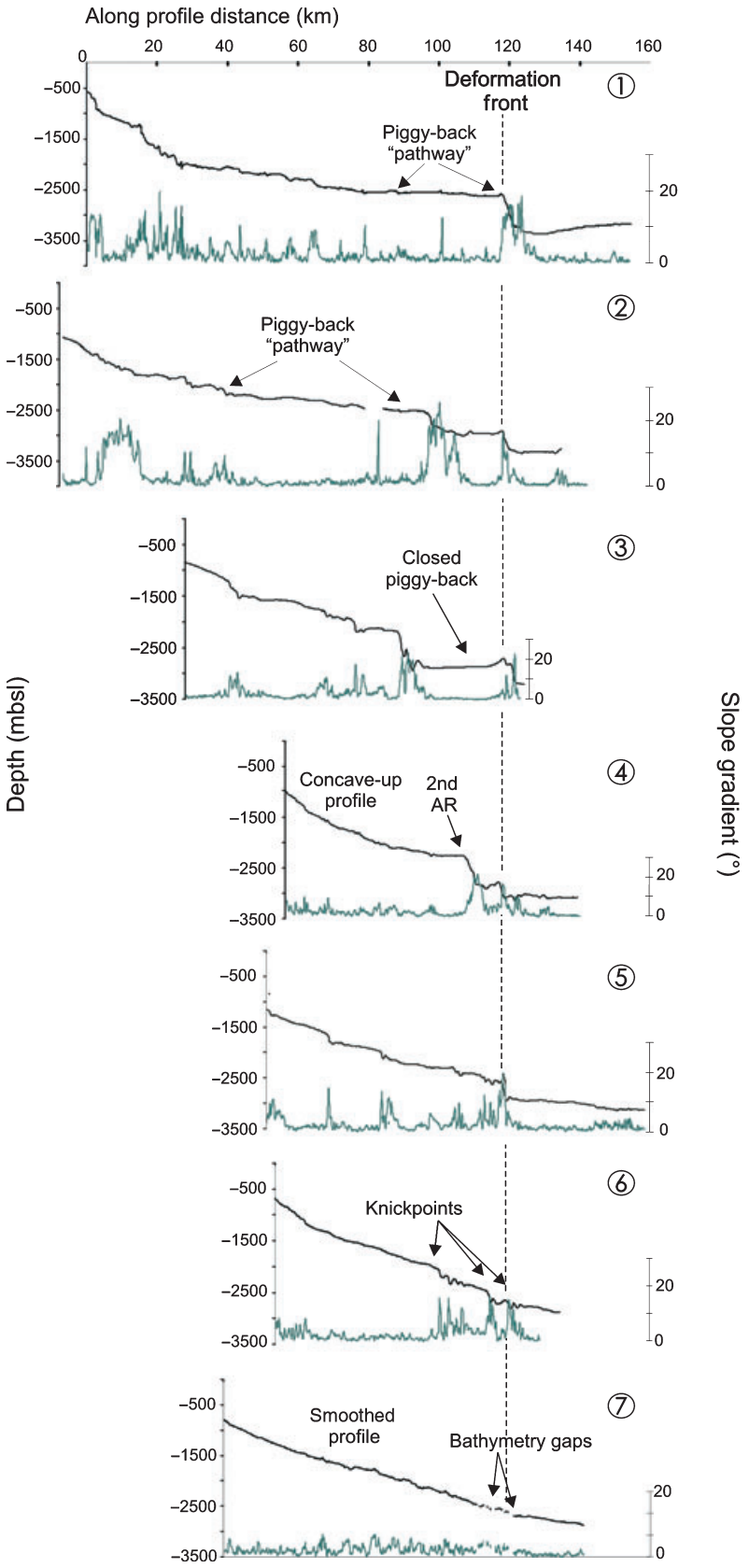

Fig 4. Longitudinal depth profiles (in m b.s.l.) and slope gradients (absolute values, in degrees) of the Makran canyons, with position of the deformation front. AR, accreted ridge. Location of profiles is shown in Fig. 2.

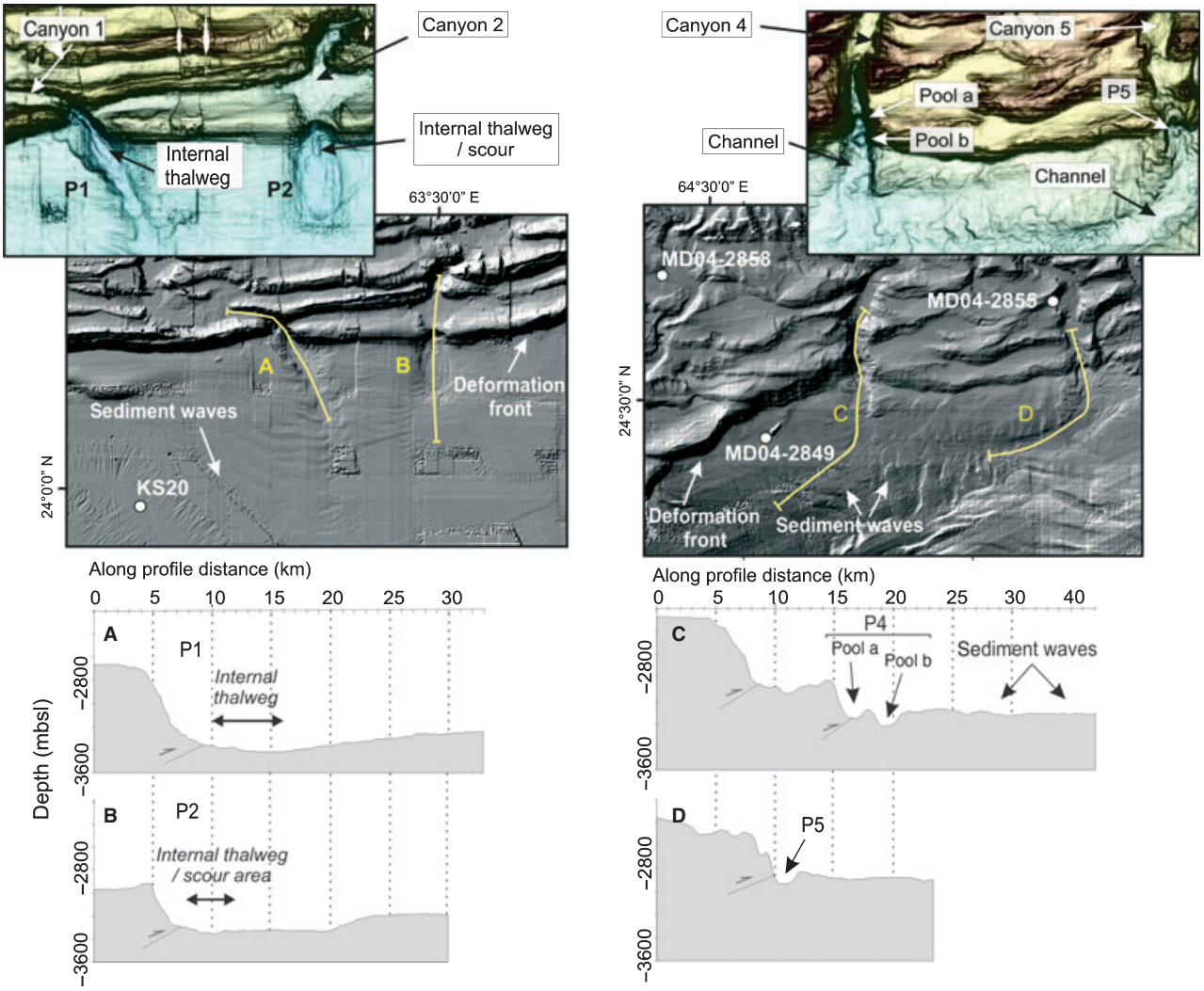

Fig. 5. Close-up views of multibeam bathymetry in the deformation front area, in the western (left) and eastern prism (right). Longitudinal depth profiles of the plunge pools located at the mouth of Canyon 1 (A), Canyon 2 (B), Canyon 4 (C) and Canyon 5 (D).

long and 66 to 125 m deep) are observed directly at the foot of the deformation front (Fig. 5). P1 is characterized by a subdued topographic rampart on its downslope side, which is partly breached near its centre (Fig. 5). Inversely, P2 is closed by a 140 m high rampart and forms a large bowl in the abyssal plain (Fig. 5). Downstream, these plunge pools are associated with the development of sediment waves radial to the flow direction (i.e. from north/south to east/west direction; Fig. 5). Sediment waves associated with P2 show wavelengths of 3 to 0·6 km and wave heights of 15 to 2 m (Fig. 6); they are of a lower order of magnitude in both wave length and wave height than those associated with P1 (i.e. 4·5 to 0·6 km in wavelengths and 25 to 5 m in wave heights).

The size of the plunge pools at the deformation front decreases towards the eastern prism (Table 3). At the mouth of Canyon 4, two successive, circular plunge pools are observed downstream of a 300 m high knickpoint (Fig. 5). The two depression zones are 80 and 140 m deep, respectively, and are 2 km wide and 2·5 km long. This plunge pool system does not close abruptly as observed for P1 and P2, and a channel develops in the abyssal plain (with a maximum size of 6 km wide and 70 m deep). This channel disappears 24 km downstream of the deformation front (Fig. 2). Sediment waves are observed on the right flank of the channel, and show wavelengths of 5·4 to 1·5 km and wave heights of 39 to 11 m (Fig. 6). Similarly, plunge pools at the mouths of Canyons 5 and 6 are only 120 m deep and <2 km long (Fig. 5). There is no major disturbance at the mouth of Canyon 7 and channel continuation is enhanced, structurally constrained to the north

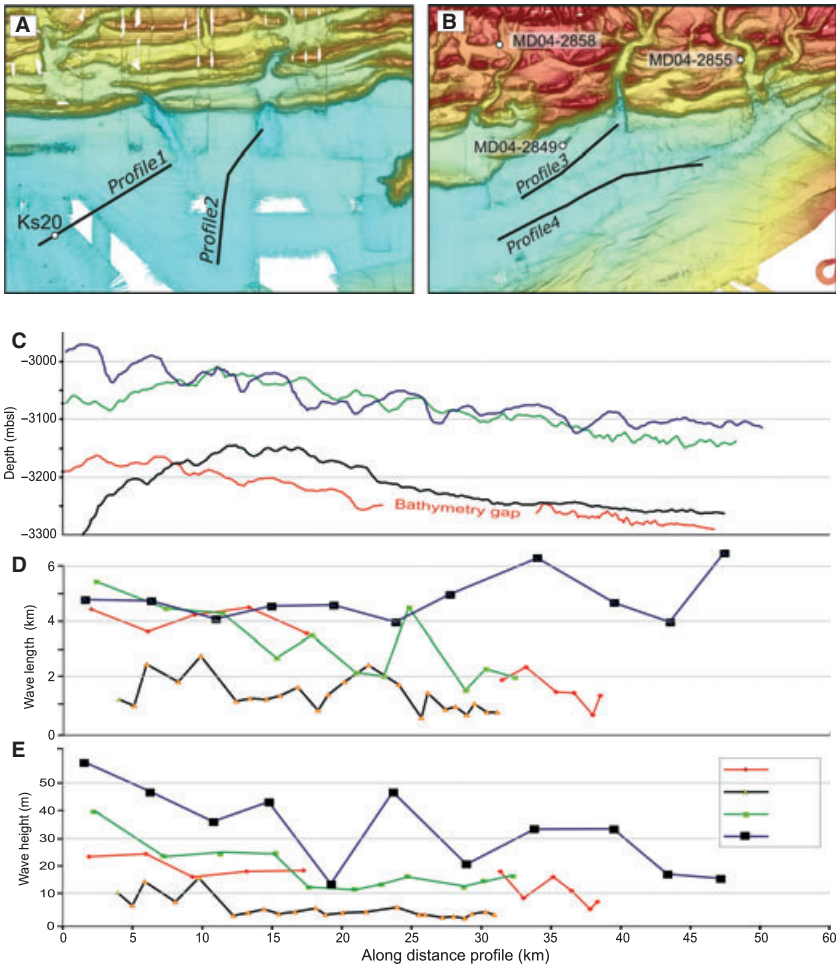

Fig. 6. Close-up views of bathymetry in the deformation front area and the sediment wave fields in the western (A) and eastern prism (B), with position of the depth profiles (C) and localization of the sedimentary cores. For each sediment wave field, wave length (km) measurements are presented in (D) and wave height (m) measurements are presented in (E).

and south by the first accreted ridge and the Murray Ridge, respectively (Fig. 2). The channel finally joins with the continuation of Canyons 5 and 6 and forms a channel with a maximum size of 8 km wide and 150 m deep. It rapidly narrows before it disappears on the bathymetry data 40 km downstream of the Canyon 7 mouth (Fig. 2). The channel is associated with sediment waves characterized by wavelengths of 4·7 to 3·9 km, and wave heights that fall between 57·5 and 14 m (Fig. 6). The sediment waves are characterized by irregular crest morphology (Fig. 6) and are organized symmetrical to the east to west trending axial channel until the latter narrows.

SEDIMENT DISTRIBUTION

Acoustic data

Piggyback basins

Piggyback basins show variable backscatter acoustic facies: most of them are characterized by a low to very low reflectivity (Fig. 7) suggesting fine-grained sediment deposition (whether it is turbidite or hemipelagites). A higher reflectivity is observed only in the western domain, where piggyback basins are connected to the canyons, and seem to act as preferred turbidity current pathways (Fig. 7). In the 'closed' piggyback at the mouth of Canyon 3 (Fig. 8), a 200 km^2 lobe of very low backscatter (black) acoustic facies is observed downstream of the knickpoint wall (Fig. 8). Here, the sediment transfer is disconnected from the abyssal plain because of uplift of the frontal fold (Mouchot *et al.*, in press). Overall, backscatter distribution along the Makran slope evolves from east to west and suggests enhanced trapping of sediments in the western slope along structural traps.

Plunge pools

The backscatter imagery shows that 'lobes' of very low backscatter (black) acoustic facies are confined within the western plunge pools (P1 and P2; Fig. 8), directly in front of canyon mouths (i.e.

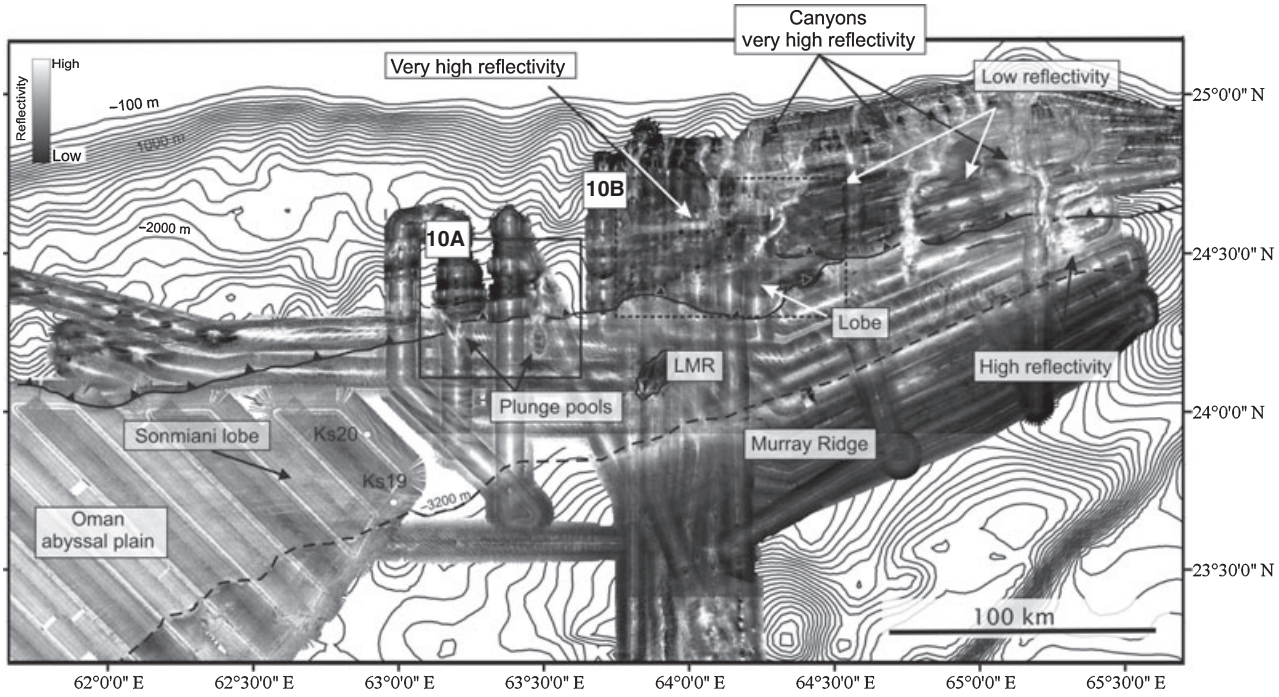

Fig. 7. Reflectivity map (12 kHz) of the study area. Data compiled from the MARABIE and CHAMAK cruises (high backscatter are in light, low backscatter in dark).

downstream of the knickpoint wall). This facies, similar to the one observed in the canyon-mouth lobe (Fig. 8), contrasts with the surrounding medium reflectivity in the abyssal plain. The backscatter imagery of the plunge pools located in the eastern Makran province is not as well-defined, partly due to their lesser extent and the poor data resolution in this area (Fig. 7). However, an overall high-backscatter (white) acoustic facies is observed downstream of the deformation front in the easternmost abyssal plain (Fig. 7).

Seismic profiles collected across P1 and P2 (Fig. 9) show that the bottom of the plunge pools is characterized by a strong bottom echo at 3·5 kHz, with no or indistinct sub-bottom reflectors, corresponding to the echo-facies Ib of Mouchot *et al.* (in press). This echo type is usually interpreted as indicating coarse-grained deposits (Damuth, 1975; Mouchot *et al.*, in press). The flanks of the plunge pools (Fig. 9) are characterized by a distinct sharp, continuous bottom echo with parallel sub-bottom reflectors, corresponding to the echo-facies Ia of Mouchot *et al.* (in press) and usually associated with fine-grained sediments (Damuth, 1975). Finally, an indistinct bottom echo with an irregular surface (echo-facies IIa) is observed along the steep internal flanks of the plunge pools, suggesting scars and/or irregular erosion surfaces (Fig. 9).

Internal morphology and distal depositional architecture of P1 is observed on the multi-channel seismic line (Fig. 10). Mass transport deposits (MTDs) are characterized by low to medium amplitude, discontinuous reflectors and a slightly chaotic facies (Fig. 10). These deposits form 50 to 100 m thick lenses (60 to 125 ms TWT), which are observed along the P1 flank (extending to a length of 2 to 2·5 km) although one MTD extends for more than 5 km in the plunge pool depression (Fig. 10). Laterally (in the plunge pool topographic depression), the MTDs are interbedded within high-amplitude, fairly continuous reflectors (HARs), that onlap the MTDs to the north/north-east (Fig. 10); to the south, they also onlap very continuous, medium-amplitude reflectors that form the plunge pool flank (Fig. 10). High-amplitude, onlapping reflectors are interpreted as distal plunge pool deposits that aggrade and migrate in a south/south-west direction. These deposits tend to form lobate complexes 20 to 50 m thick composed of sheets that can be continuous for several kilometres (Fig. 10). The thickness of the plunge pool deposits (from the incision base of the plunge pool) is about 0·25 s TWT (i.e. 200 m thick).

The Sonmiani lobe

An 86 km long and 15 km wide high backscattering area is observed in the central abyssal plain

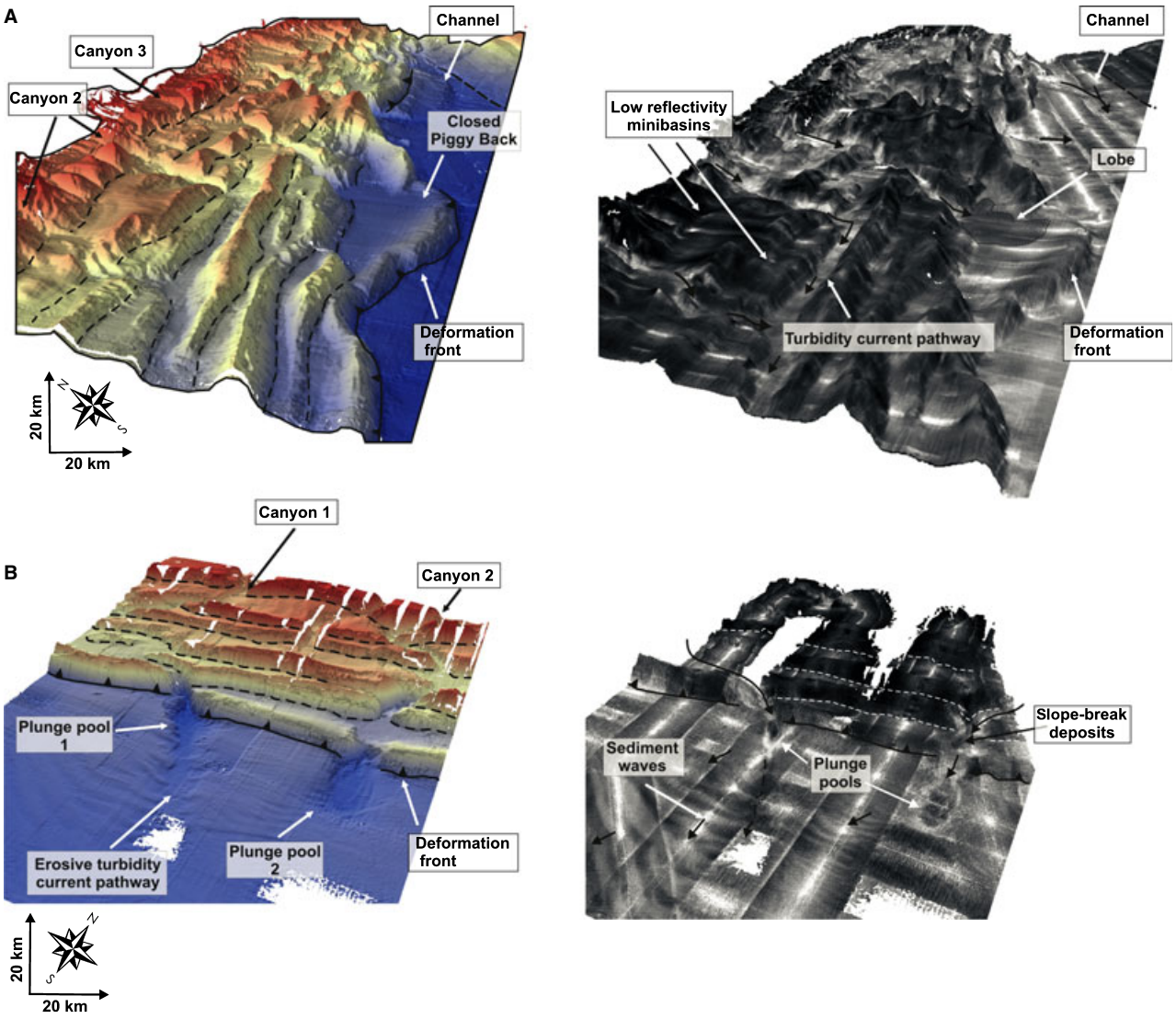

Fig. 8. Three-dimensional shaded bathymetry (left) and reflectivity maps (right) showing the low-reflectivity lobe at the mouth of Canyon 3 (closed piggyback basin) and the higher backscatter within a piggyback basin used as the Canyon 2 pathway (A); and the low reflectivity associated with plunge pools 1 and 2 in the western prism (B).

(Fig. 7), confined southward by the Murray Ridge. It consists of a proximal area of general high reflectivity with isolated and discontinuous patches of lower backscatter intensity, and a more distal area characterized by lineaments of high-backscatter intensities parallel to the possible flow direction, continuous for more than 40 km (Fig. 7). This high reflectivity area is interpreted as a turbidite lobe. The Sonmiani lobe does not appear to be connected directly to a significant feeder system, but it develops where the slope gradient decreases significantly from 0·18° to less than 0·03°, corresponding to the area where the abyssal plain enlarges and becomes unconfined (Fig. 2). Downstream of the Sonmiani lobe, the Oman abyssal plain is unchannellized (Fig. 2) and develops along very low gradients (<0·03°).

Sedimentary facies

Sediment distribution within the Makran turbidite system has been investigated on the basis of 12 sedimentary cores sampled from the upper slope to the central Oman abyssal plain (Fig. 1). Sedimentary facies and facies associations (FA) have been inferred from visual and X-ray description, grain size and geochemical analysis, and microscopic observations of thin slabs.

Hemipelagites/pelagites (H)

Hemipelagic and/or pelagic (background) sedimentation is typically observed on the bathymetric highs (for example, the Murray Ridge and the Little Murray Ridge). It is also found in thin to very thin layers interbedded within turbidite

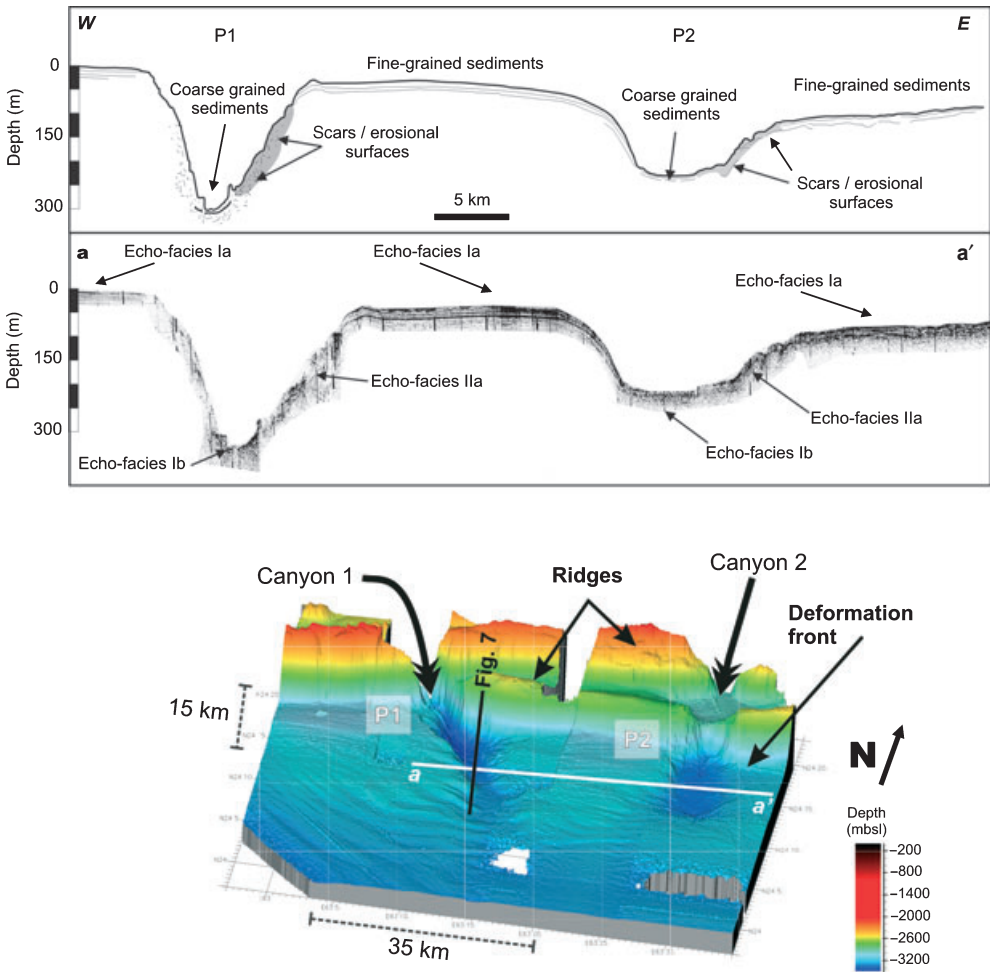

Fig. 9. Three-dimensional bathymetry of the plunge pools P1 and P2 at the mouth of Canyon 1 and Canyon 2 (western prism), 3·5 kHz seismic line (aa′) and its interpretation from echo-facies classification of Mouchot *et al.* (2010). Location of the multichannel seismic line 'Chamak 10' (Fig. 10).

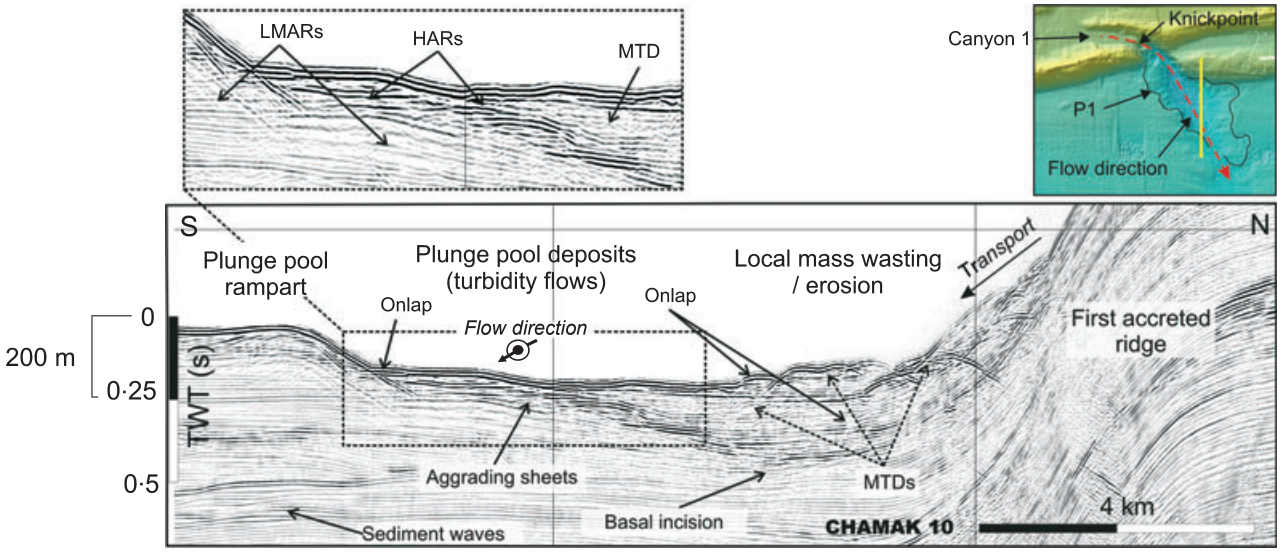

Fig. 10. Multichannel seismic line CHAMAK 10 across the plunge pool 1 (P1). HARs, high-amplitude reflectors; LMARs, low to medium amplitude reflectors; MTD(s), mass transport deposit(s). Close-up view of multibeam bathymetry in the P1 area, with location of the seismic line (right).

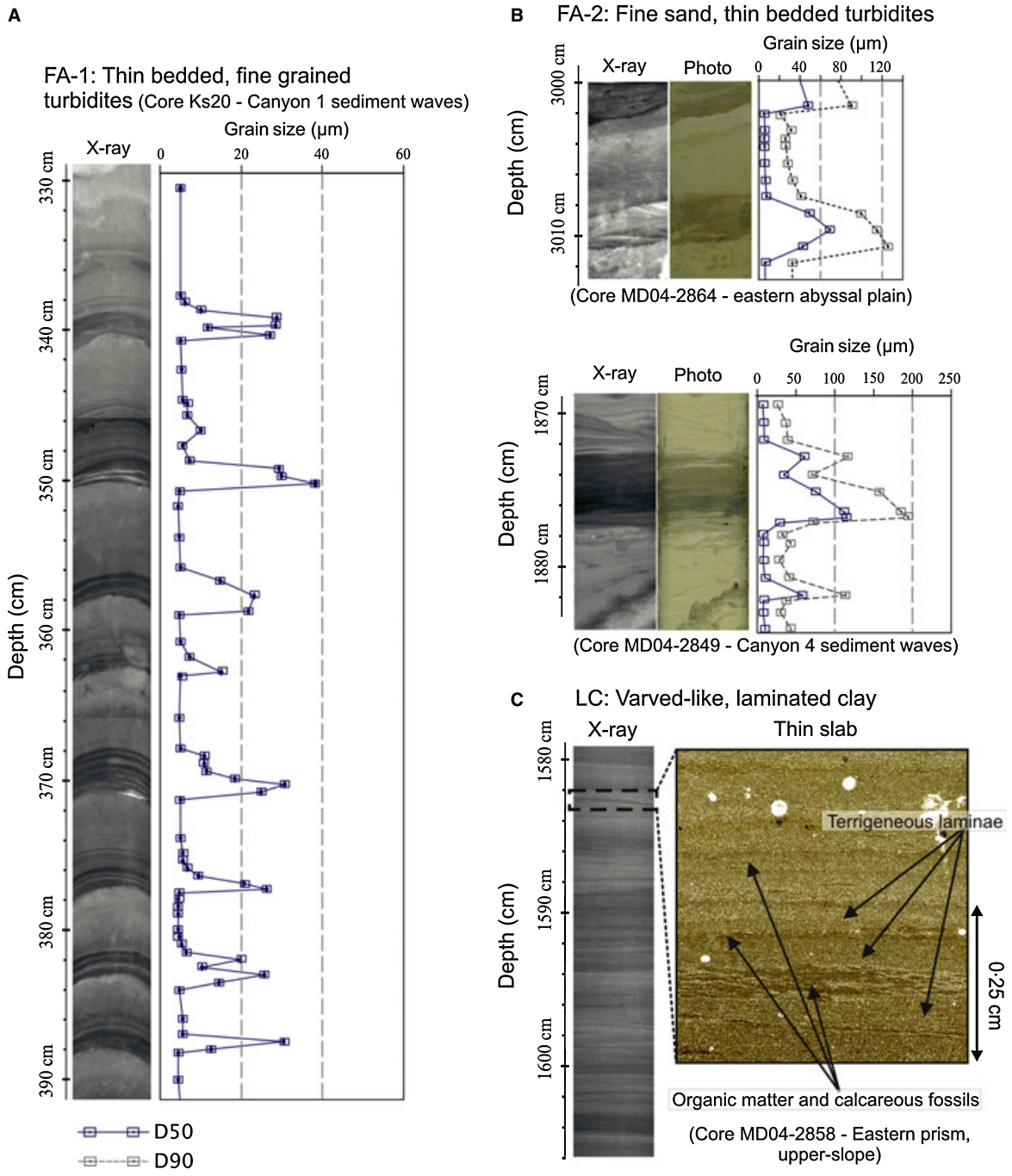

Fig. 11. X-ray pictures, photographs and grain-size measurements of the facies association FA-1a [interpreted as being silt–mud, thin-bedded turbidites; (A)] and FA-2 [interpreted as being fine sand, thin-bedded turbidites; (B)]. (C) X-ray picture and thin-slab of sedimentary facies association 'laminated clay' ('LC') observed in the upper slope (core MD04-2858). Location of cores in Fig. 1.

sediments. It mostly consists of grey to light brown, fine-grained (D_{50} <7 µm) bioturbated clay layers (Figs 11 and 12), with abundant microfossils. Bioturbation rate is variable and may depend on core location and depth, but pyritized burrows are commonly observed. Distinctive Ca-rich hemipelagites are observed in some of the cores, consisting of light grey to white bioturbated clay layers with high to very high Ca content (Fig. 13).

Laminated ('varved-like') clay (LC)

Grey olive to brown, laminated clays are the main sedimentary facies observed in core MD04-2858,

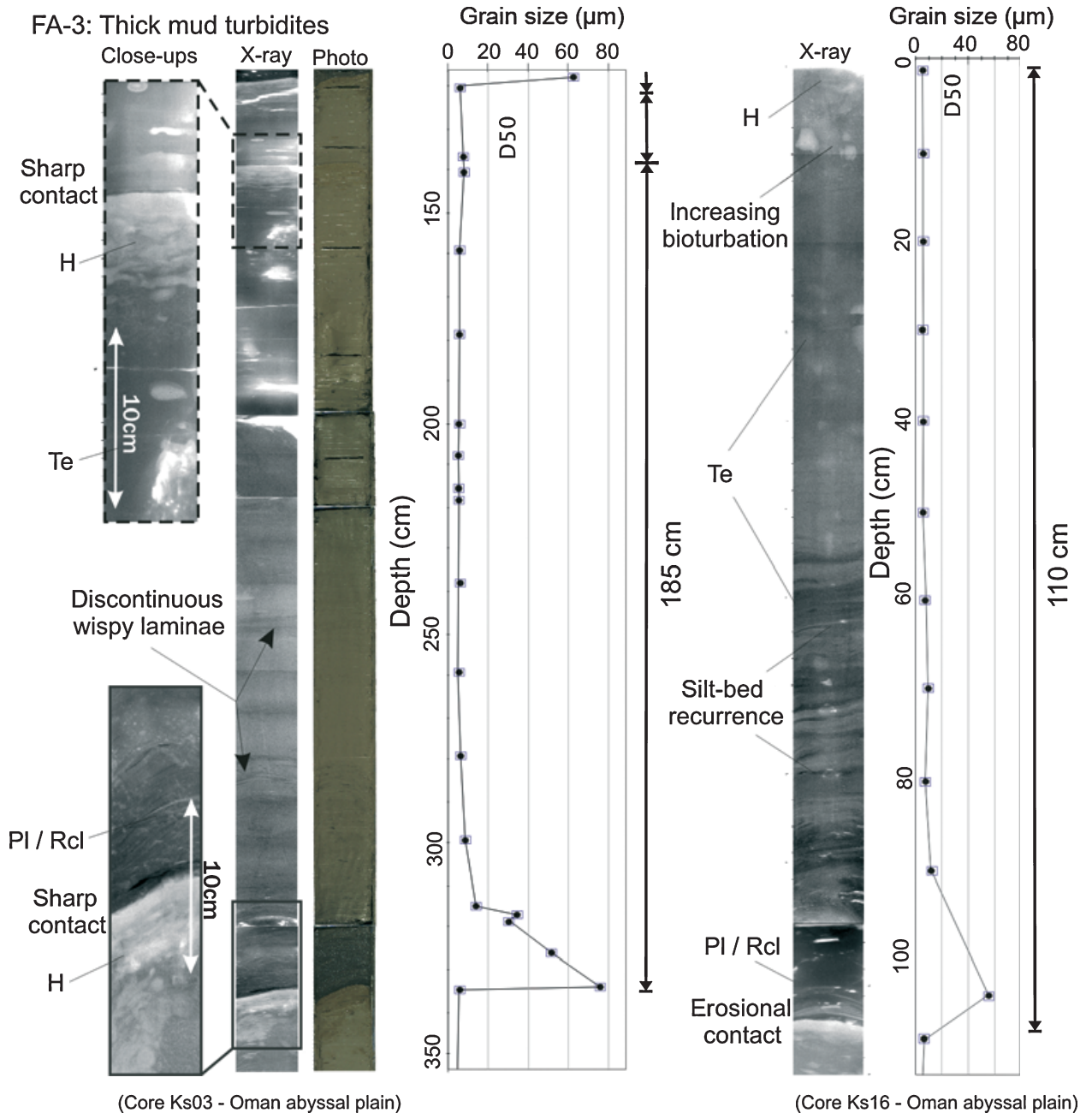

Fig. 12. X-ray pictures, photographs and grain-size measurements of sedimentary facies association FA-3 (interpreted as being thick mud turbidites), observed in the central abyssal plain. Location of cores in Fig. 1.

located in an upper slope piggyback basin (Fig. 1). It consists of an alternation of a few millimetre thick, olive-grey laminae, with abundant organic matter and biogenic calcareous fossils (Fig. 11), stacked with thinner, light grey, mostly terrigeneous laminae. This laminated facies has been described commonly in the Makran continental slope and is interpreted as 'varved-like' sediments related to river-derived deposits related to flood events (von Rad *et al.*, 1999a; Luckge *et al.*, 2001; von Rad *et al.*, 2002). In the core MD04-2858, this laminated facies is interbedded with a few centimetre thick silt-mud turbidites.

Fine-grained, thin turbidite beds (FA-1)

Facies association 1 (FA-1) consists of a basal silt layer (D_{50} <63 µm), that generally shows planar lamination, fining up into a dark grey to brown mud, with no bioturbation and very rare microfauna (Fig. 11). A sharp to slightly erosive surface is present between the underlying hemipelagite

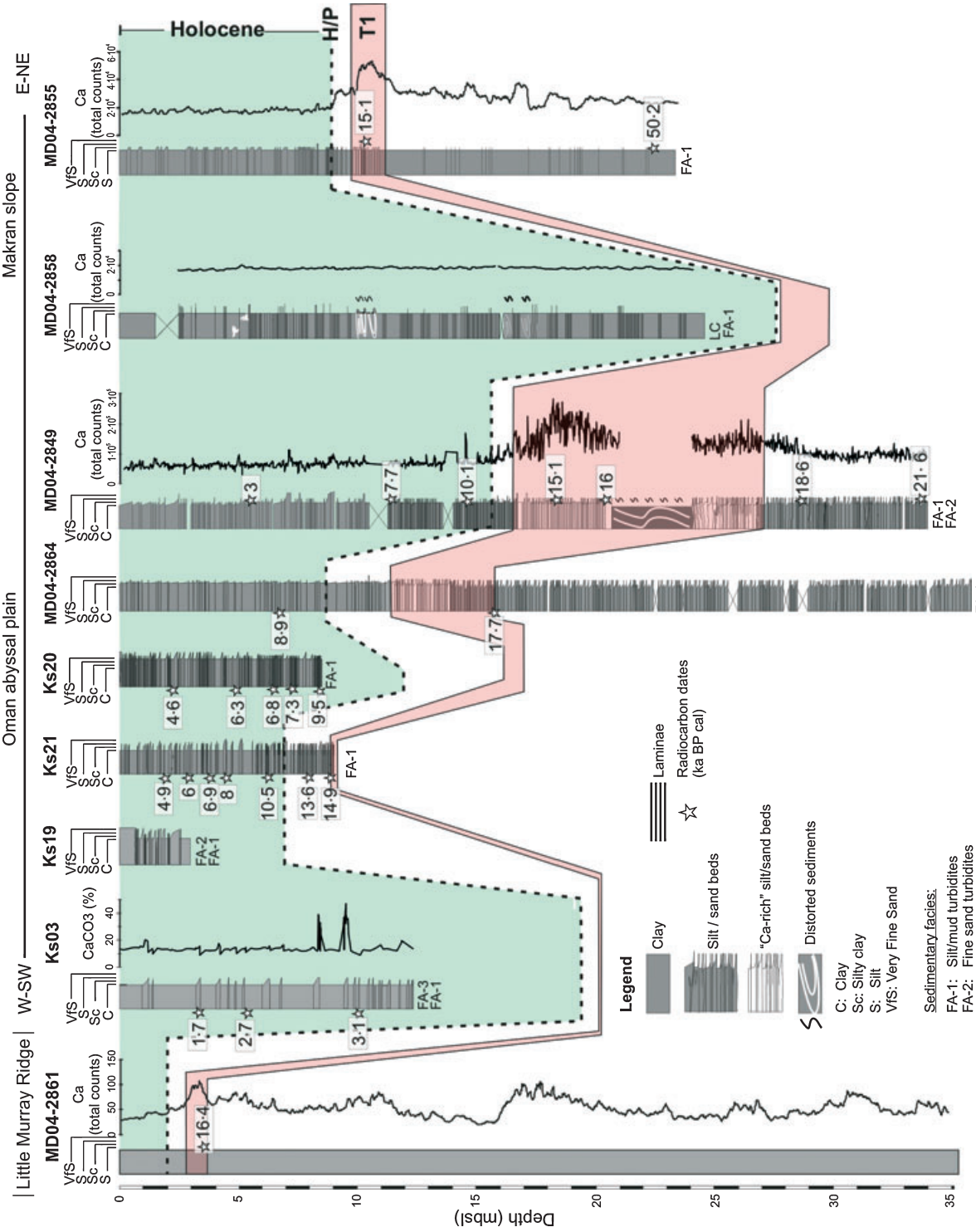

Fig. 13. Stratigraphy, sedimentary logs, Ca/$CaCO_3$ content, and correlation of the sedimentary cores from the eastern to the western Makran accretionary prism. Stars indicate the calibrated AMS-14C dates (Table 2).

and the silty bed, whereas the facies association ends with a gradual transition into hemipelagic deposits. The association FA-1 forms typical centimetre to decimetre thick fine-grained turbidites, corresponding to the T_d to T_e terms of Bouma (1962). These deposits are usually interpreted as resulting from overspilling of the upper part of a turbulent flow over turbidite-channel levées (Hesse & Chough, 1980; Piper & Deptuck, 1997), as well as deposition in distal (abyssal plain) and fringe settings. FA-1 beds mainly composed the sediment wave fields, and more generally the proximal abyssal plain. This facies association is also observed in the piggyback basin close to the Canyon 5 flank (core MD04-2855, Fig. 1).

Fine sand turbidites (FA-2)

Facies association 2 (FA-2) consists of a fine sand basal layer (D_{50} generally <130 μm) that can be either massive or with sedimentary structures such as planar or ripple cross-lamination (Fig. 11). It generally overlays hemipelagic deposits with a sharp to slightly erosive contact. The basal fine sand layer fines up into silt and mud that commonly show planar lamination (Fig. 11). The facies association is overlain by hemipelagic deposits, showing a gradual contact. Facies association 2 beds are interpreted as medium to fine-grained turbidites showing the T_c to T_e terms of Bouma (1962). Thin-bedded, <10 cm thick fine sand turbidites (Fig. 11) are observed in cores MD04-2849 and MD04-2864 (Fig. 1). Fine sand turbidites with a basal layer thicker than 10 cm are only observed in the Sonmiani lobe.

Thick mud turbidites (FA-3)

Facies association 3 (FA-3) consists of thick turbidites (up to 180 cm) composed of a millimetre to decimetre thick basal layer of very fine sand to silt ($D_{50} \sim 100$ to 50 μm), with common oblique to parallel lamination (T_c to T_d), that fines up to a thick, slightly normally graded dark brown to grey mud layer, characterized by the absence of bioturbation and microfossils, and an often complex structure with irregular silt-bed recurrence and wispy laminae (Fig. 12). The latter is interpreted as the T_e term of Bouma (1962), resulting from the decantation of the turbidity current nepheloid cloud. The gradual transition towards a light grey, bioturbated and microfossil-rich mud (hemipelagite/pelagite) is well-observed on the X-ray data (Fig. 12) allowing a precise quantification of the T_e interval thickness. The basal (coarser) sequences (for example, T_c to T_d) sometimes consist of multiple fining or coarsening-upward packages, 3 to 10 cm in thickness, composed of silt-mud laminae (Fig. 12). The sand/mud ratio within FA-3 deposits is 1:17 on average.

Core stratigraphy and sedimentation rates

Core stratigraphy and correlation has been achieved using a combination of 27 radiocarbon ages (Table 2), Ca content and lithostratigraphy. The sedimentological logs and the down-core distribution patterns of Ca XRF intensities in cores MD04-2861, MD04-2849, MD04-2855 and MD04-2858, and the absolute $CaCO_3$ content in core KS03 are shown in Fig. 13. Enhanced Ca values are recorded in discrete intervals in cores MD04-2861, MD0428-49 and MD04-2855, whereas these Ca peaks are not observed in the cores MD04-2858 and KS03 (Fig. 13). In the latter core, two single $CaCO_3$ peaks are related to two turbidite foraminifera-rich basal layers. Radiocarbon ages obtained in the Ca-rich hemipelagic intervals range between 16·4 and 14·9 kcal BP (Fig. 13). In the cores MD04-2849 and MD04-2855, they are interbedded with white to light grey turbidites (of FA-1 and FA-2), showing higher XRF Ca values (Fig 13). These sequences are also observed in the core MD04-2864, allowing lithostratigraphic core-to-core correlation (Fig. 13).

The sedimentary record of Ca peaks in both hemipelagic and turbidite deposits in the Arabian Sea has been detailed by several authors in cores from the Makran continental slope and Murray Ridge, and related to increasing preservation of pteropods in the north-eastern Arabian Sea during periods of enhanced deep convective turnover of the surface water column due to an increasing winter-monsoon intensity (Reichart *et al.*, 1998; Prins *et al.*, 1999; Klöcker & Henrich, 2006). Thus, the Ca peaks observed between *ca* 17 to 15 kcal BP correspond to a period of enhanced continental aridity and north-east monsoon intensity during the period coinciding with the end of the Last Glacial Maximum and the North Atlantic Heinrich event (Sirocko *et al.*, 1996; von Rad *et al.*, 1999b; Prins *et al.*, 1999; Pourmand *et al.*, 2004). Values of Ca content weaken towards the Holocene/Pleistocene transition at *ca* 11 kcal BP (Klöcker & Henrich, 2006) and then remain low continuously through the Holocene (Fig. 13).

Sedimentation rates (and mean turbidite frequencies) have been calculated from core stratigraphy and AMS ^{14}C dates (Fig. 13). Most of the cores from the Makran turbidite system show a

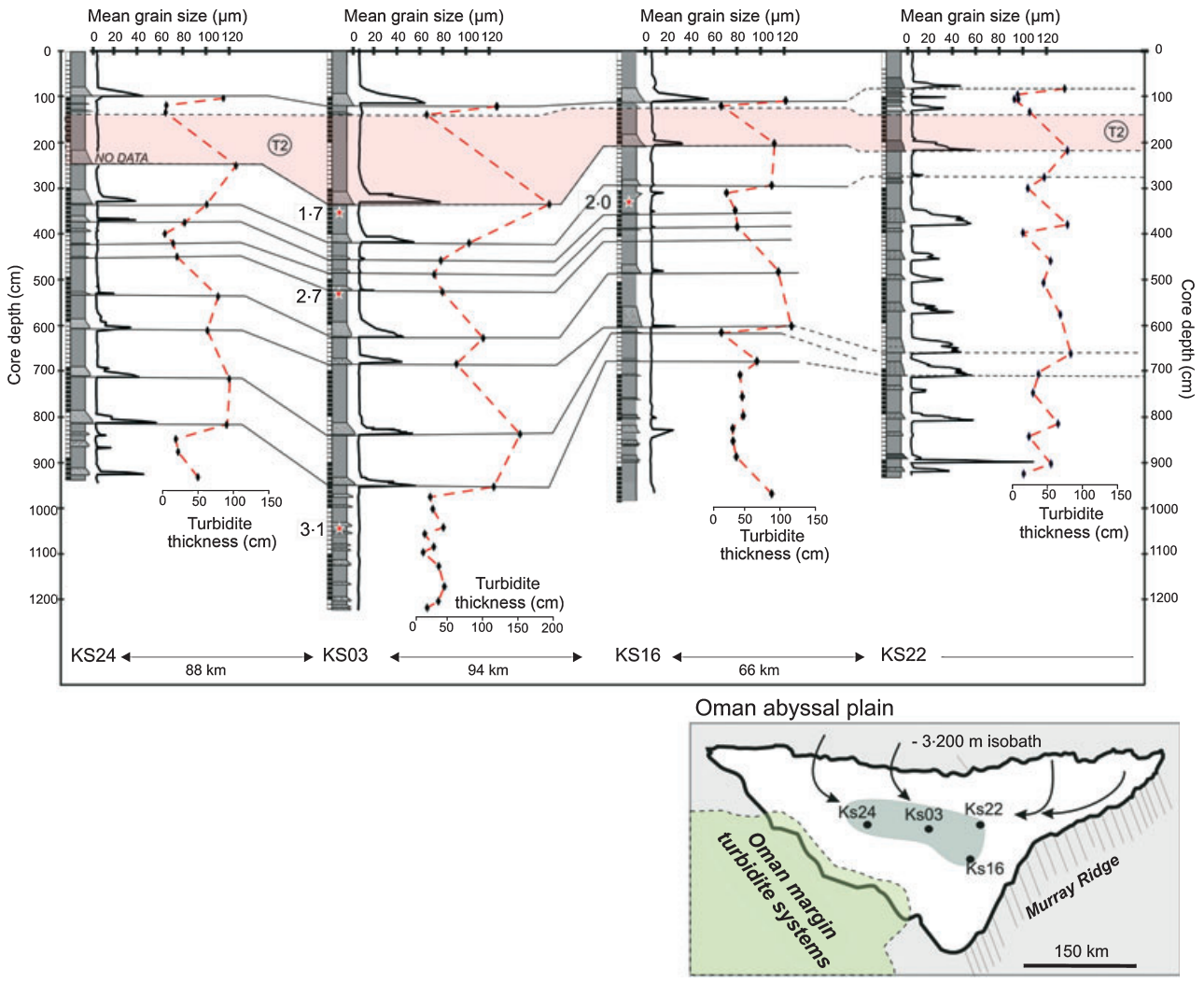

Fig. 14. Sedimentary logs, mean grain-size data (µm) and turbidite thickness (cm) that allow a 182 km long correlation of the sedimentary cores recovered in the central Oman abyssal plain. T2 represents the thickest single turbidite event recorded in the Oman basin.

thick Holocene sedimentary record (Fig. 13), and high rates of turbidite sedimentation are recorded during both sea-level lowstand and highstand periods. Late Pleistocene mean sedimentation rates at the mouth of Canyon 4 (Fig. 13) are of about 165·2 cm ka^{-1}, and remain high during the Holocene (129·8 cm ka^{-1}). Holocene mean sedimentation rates are lower at the mouth of Canyon 1 (90·9 cm ka^{-1}, core KS20) and in more distal positions (75·6 and 58·5 cm ka^{-1} in the cores MD0428-64 and KS21, respectively; Fig. 13). Very high sedimentation rates (233 cm ka^{-1} on average) are observed in the deep abyssal plain (i.e. KS03, KS16, KS22 and KS24) from a Late Holocene thick turbidite sequence (up to 10 m for the last 3 kcal BP; Fig. 14) mostly composed of FA-3 beds of low recurrence time (250 years on average). Very high sedimentation rates are also observed in the upper slope (MD04-2858), where a minimum estimate of *ca* 200 cm ka^{-1} can be inferred based on the 22 m thick sedimentary record of 'varved-like' (LC) Holocene deposits (Fig. 13).

Abyssal plain turbidite correlation

Cores from the Oman abyssal plain all show the vertical stacking of thick mud turbidites (FA-3) with rare decimetre-thick fine-grained turbidites FA-1 (Fig. 14), separated by thin hemipelagic/pelagic muds (H). Core correlation has been achieved using a detailed analysis of the sedimentary sequences including grain-size measurements, individual turbidite bed thickness and radiocarbon dating (Fig. 14). Most of the abyssal plain turbidites are well-correlated

between the cores KS24, KS03 and KS16, representing individual bed correlation along a 182 km long transect. Turbidite correlation is more unclear eastward (core KS22), although thicker beds can plausibly be correlated (Fig. 14). Indeed, the core KS22 is located in the more proximal location (only 80 km downstream of the Sonmiani lobe) and is likely to have received more frequent flows from the eastern canyon systems (Fig. 2).

Nonetheless, turbidite bed correlation shows that the gravity currents that reach the flat and unchannellized Oman abyssal plain are likely to produce extensive (sheet) turbidite deposits. Simple calculations from the thicker (114 cm on average), core-to-core correlated turbidite bed (T2 on Fig. 14) give a minimum of 4·7 km^3 of sediment that have been deposited within a single event, although the measurement error is probably large (due to the small number of cores and hence the lack of spatial control). Maximum thicknesses for individual turbidite beds are observed on the core KS03, in the centre of the basin (Fig. 14), and the turbidite beds are generally thin towards the south (KS16) and east (KS22), while the mean grain size of the turbidite basal intervals fines towards the south (KS16). Thus, most of the thick, mud-rich and unchannellized turbidity flows that cross the Oman abyssal plain are probably partially 'ponded' in the centre of the basin, while the remainder of the flows travel southward and terminate through onlap against the Murray Ridge.

DISCUSSION

Sedimentary processes on the margin

Turbidite system activity

Widely used sequence stratigraphic models (e.g. Posamentier & Weimer, 1993) postulate that turbidite system growth predominantly occurs during periods of falling sea-level and sea-level lowstand, when rivers entrench at the shelf edge. Most of the present-day passive-margin fans show reduced or absent turbidite deposition (Kolla & Perlmutter, 1993; Ducassou *et al.*, 2009), as sediment is mostly trapped on the shelf. Like several modern turbidite systems located in tectonically active settings (for example, the California borderlands fans, Normark *et al.*, 2006; the Cascadia margin; Goldfinger *et al.*, 2007), the Makran margin shows a persistent turbidite activity during the Late Holocene sea-level highstand conditions (Fig. 13). Turbidite sedimentation rates remain high in both proximal (i.e. canyon-mouth sediment waves) and distal (basin plain) locations (Fig. 13). Highstand turbidite system growth on the Makran margin is probably enhanced by important continental erosion by typical active margin rivers located in an arid environment (von Rad *et al.*, 1999a). While river mouths have been disconnected from the canyon heads since the post-glacial rise in sea-level, the occasional heavy rainfall in the hinterland lead to strong flood events in the Makran area, at the origin of the very thick river-derived (plumites) Late Holocene upper slope sedimentary sequence described by von Rad *et al.* (1999a) and Luckge *et al.* (2001) and observed in the core MD04-2858 (Fig. 13). These sediments could then be flushed occasionally to the deep basin in the form of gravity currents, either triggered by subduction earthquakes (Ambraseys & Melville, 1982) or resuspension mechanisms during monsoon storm events (Piper & Normark, 2009).

Origin of the basin plain thick mud turbidite beds

Sheet-like, thick (metric) turbidite beds, like those observed within the Oman abyssal plain (FA-3), are not usual but may occur in low-gradient (<1°), poorly channellized basin plain settings fed by large-volume flows. Examples include the Hatteras abyssal plain (Elmore *et al.*, 1979), the north-west African margin (Wynn *et al.*, 2002), the Horseshoe abyssal plain (Lebreiro *et al.*, 1997), the Mediterranean Sea (Rothwell *et al.*, 2000) and the Miocene Marnoso-arenacea Formation in Italy (Ricci Lucchi & Valmori, 1980; Talling *et al.*, 2007). In the Oman basin, the volume estimation of the largest turbidite bed correlated (T2 on Fig. 14) exceeds 4·5 km^3. Such sediment volumes are too high to be brought to the distal basin by flood-generated turbidity currents or resuspension mechanisms (Talling *et al.*, 2007), unless there is significant sea floor erosion along the flow pathway (Piper & Normark, 2009). The FA-3 beds are often characterized by a complex repetition of silt-beds and the presence of wispy laminae in the thick T_e layer (Fig. 12). Some of the FA-3 beds also show a basal sequence of several silt-mud laminae packages (Fig. 12). The overall complex internal structure, silt-bed recurrence, and great thickness of the poorly graded T_e layer suggest that the flows at the origin of such thick deposits did not occur as discrete flow but probably as successive surges occurring in a single, thick muddy turbidity current (Lowe,

1982; Kneller, 1995; Wynn *et al.*, 2002; Tripsanas *et al.*, 2004). Similar bed architecture has been observed in sheet-like, thick basin-wide turbidites at different locations and has been interpreted as the product of slump or slide-triggered, large-volume turbidity currents in which velocity, shear mixing rate or volume of failed sediment in motion vary over time (Wynn *et al.*, 2002; Talling *et al.*, 2007).

The higher Late Holocene sedimentation rates in the basin are observed in the distal abyssal plain, despite a recurrence time of thick turbidites of *ca* 250 years, that is significantly lower than the turbidite frequencies observed in the proximal abyssal plain (*ca* 100 years) for the same time span. Thus, only rare, large-volume muddy flows, probably initiated by large failures of the shelf edge and/or upper slope fine-grained sediments, occasionally reach the centre of the Oman basin during the Late Holocene highstand conditions. The resulting FA-3 beds are mostly composed of thick T_e muds, and the silt/sand bases ($T_{c\text{-}d}$) are typically millimetre to decimetre-thick, i.e. not more than those observed in the proximal cores (FA-1 or FA-2 beds). Hence, the absence of FA-3 beds in proximal areas could highlight the high efficiency of mud-rich gravity currents during the Late Holocene, in which the finer-grained component mostly bypasses the slope and the base of slope and can be transported further downstream in the central abyssal plain. Fine sand deposits observed in the Sonmiani lobe probably results from the residual deposition of such large-volume flows, where the abyssal plain enlarges and gradients are reduced.

Influence of sea floor topography on the sedimentary processes at break of slope: the plunge pools

Variations in slope topography exert a potentially major influence on sediment deposition (Pickering *et al.*, 1989), by controlling the non-uniformity of the gravity currents or by confining (ponding) them (Kneller & Buckee, 2000). Abrupt gradient changes modify the driving buoyancy force of turbidity flows, and generate local flow structures that will affect the rates of transport, erosion and deposition (Gray *et al.*, 2005). The presence of submarine plunge pools of variable size and shape at the base of the Makran continental slope illustrates the impact of the tectonically induced, complex sea floor topography on turbidite system architecture and mechanisms of sediment transfer at the deformation front (i.e. the trench-fill mechanisms). Due to the lack of seismic or core data in present-day examples of submarine plunge pools, their mechanisms of formation and the sedimentary processes within are still poorly understood. Lee *et al.* (2002) showed that submarine plunge pools at the base of the New Jersey and California continental slope occur where the decrease in slope exceeds 4°. These authors proposed two scenarios for the formation of plunge pools. Firstly, they could be related to the formation of hydraulic jumps at the break of slope, i.e. a change in the hydraulic regime from supercritical (i.e. for a Froude number, $Fr > 1$) to subcritical conditions ($Fr < 1$). Increase in turbulence in the vicinity of a jump could account for enhanced erosion and scouring (Komar, 1973; Garcia & Parker, 1989; Garcia, 1993; Waltham, 2004), while enhanced sediment deposition (related to flow deceleration and loss of capacity) occurs downstream. For given magnitudes of flow depth, density and frictional forces, there is a critical change in slope at which hydraulic jumps can occur (theoretically ranging from *ca* 0·05° to 1·2°; Komar, 1971). On present-day bathymetry, slope gradients are generally 7° to 12° in the proximal part of the knickpoint walls; they decrease towards *ca* 2 to 3° near the base of slope and, finally, abruptly fall under 0·8° to 0·5° immediately downstream of the knickpoint walls, where plunge pools form. Such important changes in slope probably enhance the formation of hydraulic jumps when flowing across the first accreted ridge. The second hypothesis proposed by Lee *et al.* (2002) refers to the impact of high-momentum sediment-laden density flows, which could excavate a depression (in a similar way to those observed for subaerial snow avalanches) and depose poorly sorted sediment downslope. Both processes may coexist and are not mutually exclusive (Lee *et al.*, 2002).

The plunge pools observed in the eastern prism (P4 to P6) range within the maximum scales of structures described by Orange (1999) or Lee *et al.* (2002) in both the New Jersey and California base of slope (i.e. ≤100 m deep, ≤4 km long and *ca* 0·4 to 2 km wide) and could be related to both hydraulic jumps and flow impact, or a combination of those mechanisms. Conversely, the size and depth of the western plunge pools (P1 and P2) are of a considerably higher order of magnitude than those previously described. Seismic lines available in this area (Fig. 10; Ellouz-Zimmermann *et al.*, 2007b) show that these large-scale features do not result from incision

through an incipient frontal anticlinal uplift (i.e. seaward propagation of the deformation front). Hence, their formation is more likely to be related to flow transformations at the break of slope. The observation of internal thalweg or scour directly downstream of the knickpoint wall in P1 and P2 (Fig. 5) indicates turbidity current erosion at the break of slope, either related to flow transformation across hydraulic jumps (Garcia & Parker, 1989; Garcia, 1993; Gray *et al.*, 2005) or repeated flow impacts (Lee *et al.*, 2002). Downstream, the high-amplitude reflection packages observed on both 3·5 kHz and multichannel seismic data suggest that the bottom of the western plunge pools (P1 and P2) constitute areas of preferential accumulations of coarse-grained deposits (Figs 9 and 10). On multibeam imagery, this echo type correlates with the very low backscatter record (Fig. 8), which is also observed in the very low-reflectivity lobe at the mouth of Canyon 3 (Fig. 8). Although low reflectivity at 12 kHz generally is associated with fine-grained deposits, past work has proved that very low backscatter intensities at high frequencies (12 to 30 kHz) could correlate with coarse-grained turbidite deposits in channel-mouth lobes (Unterseh, 1999; Auffret *et al.*, 2000; Kenyon *et al.*, 2002; Bonnel, 2005; Migeon *et al.*, submitted). Enhanced sediment deposition (Fig. 15) could be related to the decrease in both bed shear stress and current velocity downstream of the break of slope (Komar, 1973; Garcia & Parker, 1989; Mulder & Alexander, 2001; Kubo & Nakajima, 2002; Waltham, 2004; Toniolo & Cantelli, 2007; MacDonald *et al.*, 2009). While coarse-grained deposition probably occurs inside the western plunge pools, sediment waves downstream of P1 are only composed of very fine grained (silt to mud) turbidites (core KS20;

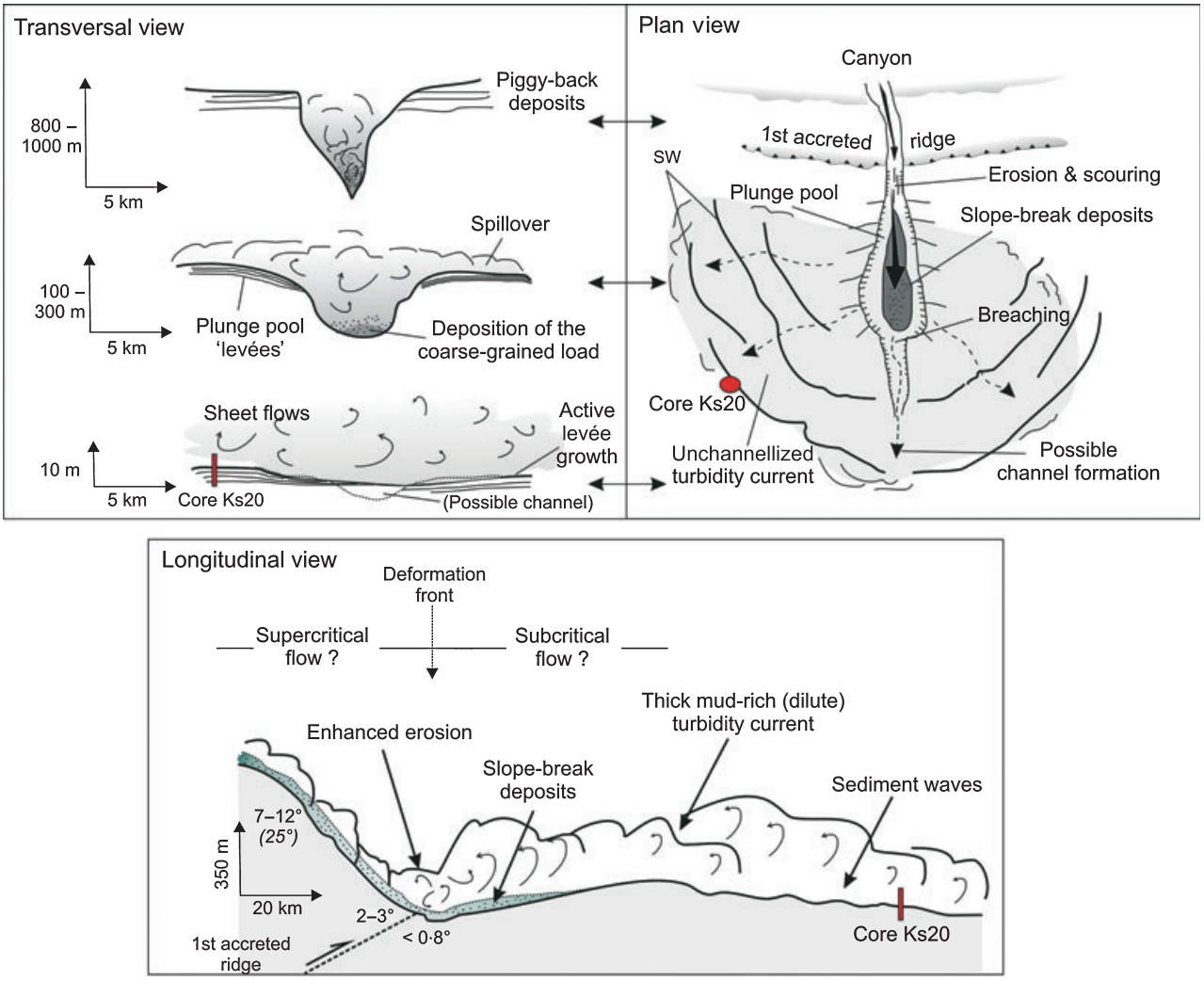

Fig. 15. Interpretative cartoon showing the sedimentary processes within the plunge pools at the deformation front. See text for explanation.

Fig. 11); this indicates that sediment waves associated with P1 are built by turbidity currents that spill over the plunge pool relief. According to the continuity equation of water flux, the rapid reduction in flow velocity is combined with an increase in flow thickness (Komar, 1971), allowing the overspill of the uppermost, finer-grained component of the turbidity flows above the plunge pool relief and flow expansion in the abyssal plain (Fig. 15). Sediment waves observed downstream of P1 indicate that such flows must be more than 300 m thick (Fig. 15), or that they were fast enough to move upslope. The resulting mechanism is similar to the classical spillover of the upper (turbulent) part of the gravity flows across the levées of turbidite channels (Piper & Normark, 1983) whereas, in the case of plunge pools, the basal part of the gravity flows stops more or less abruptly as it passes through the deformation front, while the upper part of the flows expands on the 'levées' not only orthogonal but also radial to the channel axis (Fig. 15). Thus, sediment segregation occurs at the break of slope in the western Makran turbidite system.

Although the present data provide insights into sedimentary processes within the plunge pools, it is not sufficient to understand their mechanisms of initiation and evolution over time, which probably depend on several parameters including tectonics (uplift and subsidence rates, stability of the feeder canyon) and sediment supply (nature and frequency of the gravity currents and their evolution over time). However, these 150 to 300 m deep plunge pools may result from progressive aggradation of turbidite 'levées' downstream of the break of slope, where gravity currents become more depositional (Fig. 15); this might cause gradual entrenchment of the axial depression, similar to classical submarine channels (e.g. Galloway, 1998). The observation of a breach in the downstream side of P1 indicates axial erosion of the plunge pool by energetic turbidity flows. This erosion leads to the formation of an erosive turbidity current pathway (Figs 8 and 15) cutting the field of sediment waves. Such an erosive pathway, also described along the plunge pools of the US continental slope (Lee *et al.*, 2002), may result in downstream channel initiation. However, the strong upstream break of slope (maintained by the permanent uplift of the first accreted ridge) might cause continuous base-level change, not compensated enough by sea floor erosion, which could prevent channel formation in the abyssal plain. Nevertheless, more data are needed in order to understand the mechanisms of plunge pool formation. If significant trapping of coarse-grained sediments occur within the plunge pools, they could potentially form substantial reservoirs in hydrocarbon-bearing subsurface successions. However, this possibility would depend on their longer term evolution and preservation (including the accretionary conditions).

Influence of along-strike variability in tectonic regime and fluvial input on dynamics and architecture of the Makran turbidite system

The Makran turbidite system is characterized by a strong architectural and depositional variability along strike probably related to the west to east variations in tectonic regime and characteristics of sediment supply (i.e. fluvial input, frequency of the gravity flows). Average continental slope gradients increase from west (*ca* 1°) to east (*ca* 2°), associated with shortening of the offshore prism length (from 90 km long in the western prism to 65 to 75 km long in the central and eastern prism) and a shallowing of the deformation front depth (*ca* 3150 m b.s.l. in the western prism, *ca* 2600 m b.s.l. to the east; Fig. 16). It is also associated with a decrease in length and distance between each thrust from west to east (Ellouz-Zimmermann *et al.*, 2007b). Enhanced uplift in the eastern prism could be related to changes in accretionary conditions related to décollement level position (Kukowski *et al.*, 2001), as well as the incorporation of seamounts into the subduction zone (Ellouz-Zimmermann *et al.*, 2007b). The LMR interacts with the accretionary wedge and causes general uplift of the eastern wedge as well as stacking of thrust faults and steeper slopes of the frontal structure (Ellouz-Zimmermann *et al.*, 2007b; Mouchot, 2009).

The regional distribution of fluvial input is also constrained by the structural pattern of the Makran accretionary prism: to the west, the drainage system is composed mainly of small streams (Fig. 1), with limited drainage basins of 200 to 5000 km^2 sourced in the coastal accretionary ridges. Inversely, larger mountainous rivers fed the eastern prism, particularly the Hab River, the Bela drainage basin and the Hingol River (with watersheds of 10 000 to 47 000 km^2), which converge in the Sonmiani Bay area (Fig. 16). These fluvial systems are sourced from the high-relief Makran border and Kirthar ranges which structurally correspond to the tectonic triple-

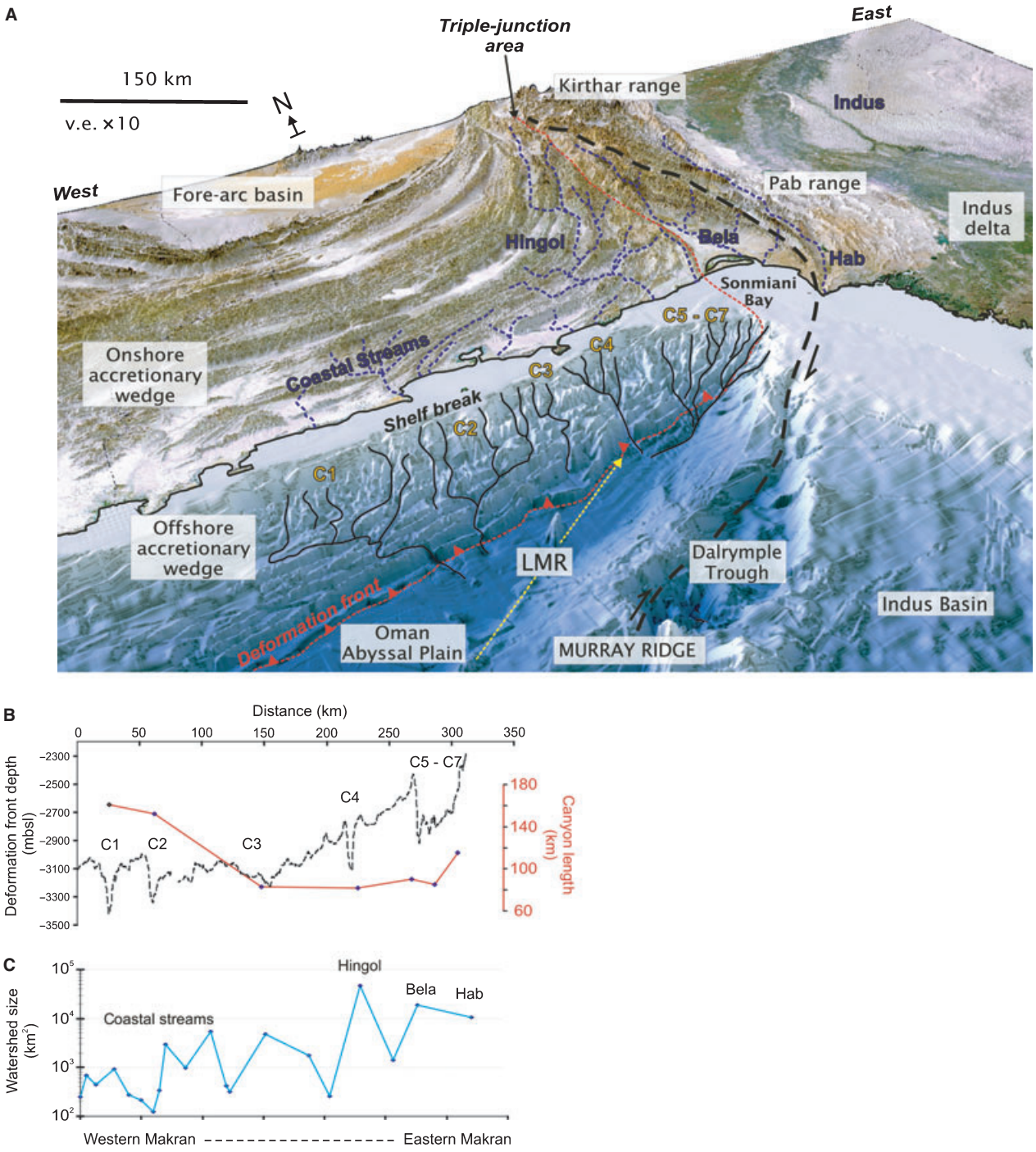

Fig. 16. (A) 3D onshore topography (SRTM data) and offshore bathymetry (MARABIE and CHAMAK cruises merged with the ETOPO 1 database) of the Makran accretionary prism, showing the structural organization of the margin. Significant streams/rivers and submarine canyons are drawn. Note the shallowing of the deformation front depth (red line) towards the east, joining the western edge of the India plate in the triple-junction area (simplified after Ellouz-Zimmermann *et al.*, 2007b; Mouchot, 2009). (B) Along-strike evolution of the depth of the deformation front (black dashed line) and the length of the Makran submarine canyons (red continuous line). (C) Along-strike evolution of the Makran watersheds size (km^2). Note that the largest watersheds are confined in the eastern Makran and Kirthar range, corresponding to the triple-junction area where the higher reliefs are observed.

junction area, where regional highs are constrained (Fig. 16). Assuming a linear relationship between the size of drainage basins and sediment discharge (Milliman & Syvitski, 1992), the sedimentary delivery to the Oman basin is likely to be considerably higher in the eastern Makran in

comparison with that in its western counterpart, where the area of the drainage basins is 10 to 200 times smaller (Fig. 16). This observation is congruent with the higher turbidite frequencies calculated by Bourget *et al.* (in Press) at the deformation front in the eastern prism (one turbidite each 31 years on average) in comparison with that in the western prism (one turbidite each 62 years on average), during the Early Holocene period (i.e. at times when rivers were still connected to the submarine canyons and, hence, probably dominantly controlled the timing of sediment delivery to the deep basin).

The combined erosional and depositional action of gravity flows tend towards theoretical 'equilibrium' conditions of the sedimentary transit systems, i.e. with a local slope such that the sediment discharge is carried along the slope with minimum erosion or aggradation (Pirmez *et al.*, 2000; Prather, 2003). Where gradient changes are imposed along a channellized system, headward erosion (and generally upstream migration) is enhanced along the steep segment, while deposition rates downstream gradually increase relative to erosion rates as gradients decrease (Toniolo & Cantelli, 2007; Mitchell, 2006). This concept of 'equilibrium profile' is illustrated in the along-strike variability of the Makran turbidite system architecture, at both large (continental slope) and small (architectural element) scales of observation (Fig. 17): the rate (and style) of tectonic deformation probably

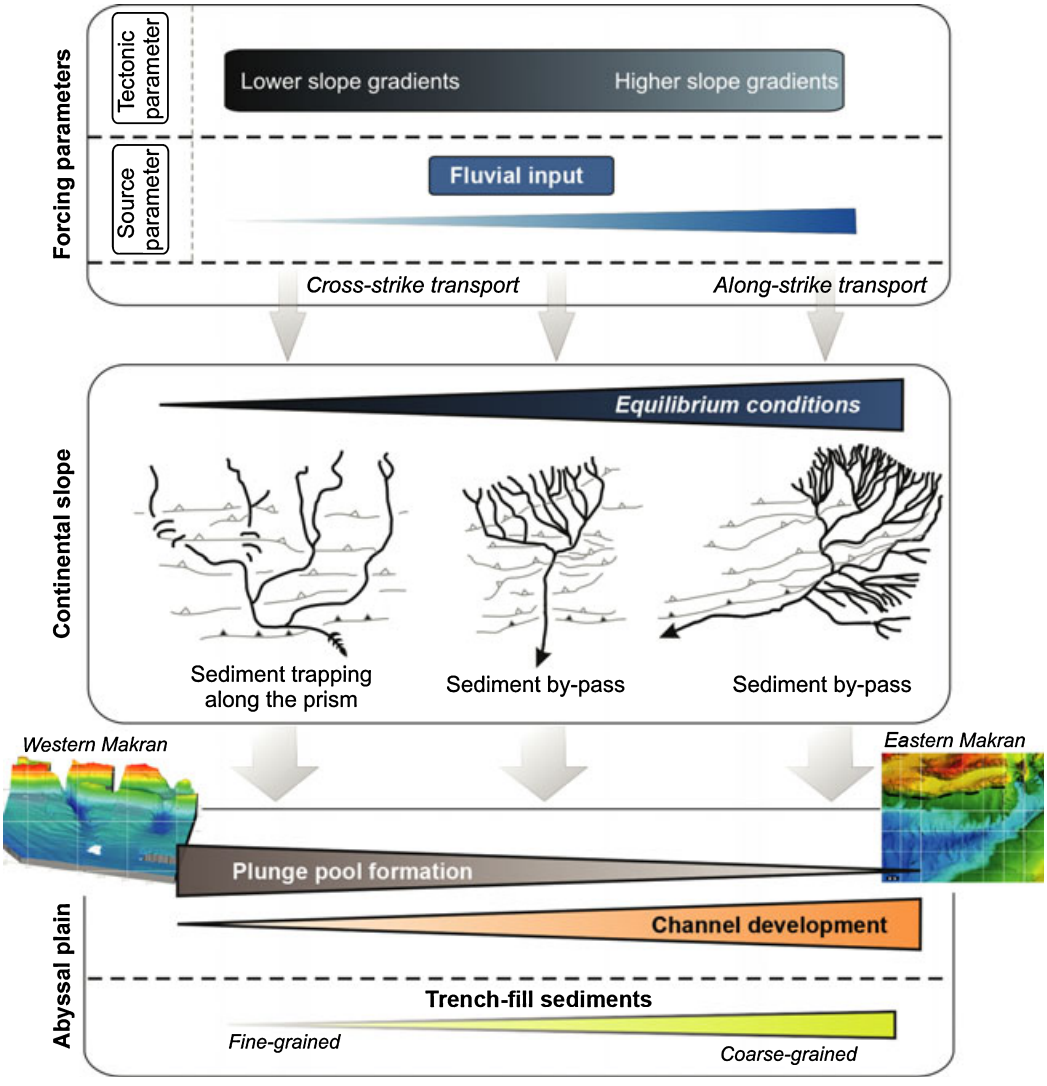

Fig. 17. Summary of the impact of the variability of the forcing parameters (tectonics and fluvial input) on the theoretical 'equilibrium' conditions of the Makran canyons, and its implication for sediment distribution and turbidite system architecture at large (continental slope) and small (architectural elements in the abyssal plain) scales of observation.

exceed the erosion rates in the western prism, where canyon morphology is highly controlled by the accreted ridges. At the scale of the continental slope, these conditions are associated with lesser prism incision, longer transit systems (Fig. 16) and enhanced trapping of the sediments along the continental slope, as the canyons follow and connect the piggyback basins (Figs 2 and 8). Active turbidite deposition, inferred from reflectivity data (Figs 7 and 8), has also been observed in cores from these western piggyback basins (Prins *et al.*, 1999; Stow *et al.*, 2002). Downstream of the deformation front, the transfer of sediment to the trench is limited to the finer-grained fraction, whereas a significant part of the sediment load is probably trapped along the wide plunge pools at the break of slope (Fig. 17). Development of very large (closed) plunge pools in this area suggests that erosion rates (i.e. sediment flux) near the deformation front are too low to compensate for the disruption in equilibrium, or there is a systematic change in the sediment flux compared with the prevailing conditions (Pirmez *et al.*, 2000), such that channels do not form. The importance of tectonic deformation in comparison with sediment flux is illustrated even more clearly in the case of Canyon 3 (Fig. 2), which is disconnected from the abyssal plain and feeds a closed piggyback basin, where a sediment fan develops (Fig. 8). Conversly, steeper gradients and higher fluvial input in the eastern domain enhanced erosion in the prism, with sediments mostly transferred towards the trench through the deeply incised, mostly rectilinear canyons. Canyon entrenchment in this area does not allow large volumes of flow overspill into the piggyback, as suggested by the low turbidite record observed on the core MD04-2855 (Fig. 13). Canyons 4 and 5 cross perpendicular to the ridges, and their longitudinal profiles suggest that the erosion rates are not efficient enough to significantly reduce the disruption relative to the canyon profiles (in particular near the deformation front; Figs 3 and 4), but the latter might be high enough to relatively smooth the morphology at the abyssal plain transition and form smaller, lower relief plunge pools with channel continuation (Fig. 17). The smooth profile of Canyon 6 (Fig. 4), characterized by a very dense network of tributaries located off a high fluvial input area (Fig. 16), suggests higher erosion rates and closer to theoretical 'equilibrium' conditions. Such conditions of the sedimentary transit system are nearly reached in the case of Canyon 7, which trends parallel to the ridges: gravity currents can bypass the deformation front and flow into the abyssal plain without major slope break, plunge pools do not form and an erosive channel develops (Fig. 17). It is associated with coarse-grained sediment waves (Mouchot *et al.*, in press), characterized by high backscatter on multibeam imagery (Fig. 7). These sediment waves are also larger (in both wave height and wavelength) than the sediment waves associated with P1 and P2 (Fig. 6). Thus, the erosional conditions reached in the eastern canyons are associated with enhanced channel development and transfer of bulk material in the trench (Fig. 17).

Thus, the Makran active margin illustrates the relationships between margin-scale structural organization (along-strike variability, location of the triple-junction area), physiography (distribution, relief and extension of the drainage basins, submarine slope gradients and morphology) and their impact on deep-water sedimentation at both turbidite system scale (canyon morphology, connection of piggyback basins) and architectural element scale (channels versus plunge pools).

CONCLUSION

The Makran active margin constitutes an excellent modern analogue to deep-water sedimentary systems in convergent margin settings. It is characterized by important turbidite activity which has remained very active during the Late Holocene sea-level highstand. This highstand turbidite sedimentation is associated with sheet-like, thick (metric) turbidite beds, which could be correlated for more than 200 km along the unchannellized Oman abyssal plain. These beds are interpreted as the result of occasional flushing of the mud-rich, river-derived sediments accumulated along the shelf edge and the upper slope, with very high Holocene sedimentation rates. The Makran margin also provides other evidence of how complex submarine slopes can interplay with the sedimentary processes and control turbidite system architecture and sediment distribution. Thrust-induced changes of gradients at the deformation front enhance substantial sea floor erosion, rapid sediment deposition, leading to the formation of unusual architectural elements, the plunge pools. Some of the plunge pools described in the Makran turbidite system are considerably larger than those previously observed along the California or New Jersey margins. Although their mechanisms of initiation and evolution over time

are still unknown, the present data provide the first insights into their internal architecture and the sedimentary processes within. Large plunge pools are associated with sediment segregation at the base of slope: large scoured areas at the slope break are followed by enhanced sediment deposition downstream. High-amplitude reflectors are observed inside the plunge pools, while their flanks are composed of thin-bedded, fine-grained turbidites deposited by the uppermost, finer-grained component of the turbidity flows.

However, the base of the Makran continental slope displays a wide range of plunge pool sizes and morphologies, varying along strike. Large plunge pools develop in the western prism, at the mouth of structurally controlled, sinuous canyons that feed and connect the piggyback basins. This configuration suggests that deformation rates exceed the erosion rates in this area, where the canyons are fed by sediments from intermittent coastal streams with low relief and very small watersheds. Considerably larger, higher relief watersheds feed the eastern Makran, where continental slope gradients are also steeper. In this area, more smoothed longitudinal profiles along the rectilinear submarine canyons indicate higher erosion rates down the slope. At the deformation front, these canyons are associated with enhanced channel formation and transfer of bulk material to the trench. Hence, the Makran accretionary prism illustrates the influence of margin-scale structural conditions on turbidite system architecture at large (continental slope) and small (architectural elements) scales of observation.

ACKNOWLEDGEMENTS

We thank IFP and SHOM for making its data available. We are indebted to all scientists, technicians and crew members of the *R/V Le Suroît, R/V Atalante* and *R/V Marion-Dufresne* for technical assistance during the MARABIE and CHAMAK cruises. The authors are also grateful to E. Moreno at the MNHN, and J. St Paul, G. Chabaud and B. Martin (University of Bordeaux) for their logistical and technical assistance. We finally acknowledge the 'ARTEMIS' project for radiocarbon dating and the 'Action Marges' French Consortium. Detailed and constructive reviews by D.J.W. Piper, R.U. Smith, P. Talling and two anonymous reviewers greatly improved earlier versions of the manuscript. Julien Bourget's PhD thesis has been funded by a DGA (French Ministry of Defense) – CNRS doctoral fellowship. This study is a UMR CNRS 5805 EPOC (University Bordeaux 1) contribution (no. 1734). The contribution by JB forms Centre for Tectonics, Resources and Exploration (TRaX) record #98.

REFERENCES

Ambraseys, N.N. and **Melville, C.P.** (1982) *A History of Persian Earthquakes*. Cambridge University Press, Britain, 219 pp.

Auffret, G., Zaragosi, S., Voisset, M., Droz, L., Loubrieu, B., Pelleau, P., Savoye, B., Bourillet, J.-F., Baltzer, A. and **Bourquin, S.** (2000) Premières observations sur la morphologie et les processus sédimentaires récents de l'Eventail celtique. *Oceanol. Acta*, **23,** 109–116.

Bard, E. (1998) Geochemical and geophysical implications of the radiocarbon calibration. *Geochim. Cosmochim. Acta*, **62,** 2025–2038.

Beaubouef, R.T. and **Friedman, S.J.** (2000) High resolution seismic/sequence stratigraphic framework for the evolution of Pleistocene intraslope basins, western Gulf of Mexico: depositional models and reservoir analogues. In: *GCSSEPM Foundation 20th Annual Research Conference, Deep Water Reservoirs of the World*, 3–6 December 2000, pp. 40–103.

Bonnel, C. (2005) *Mise en place des lobes distaux dans les systèmes turbiditiques actuels: analyse comparée des systèmes du Zaïre, Var et Rhône*. Thèse de doctorat, Université Bordeaux 1, 314 pp.

Bouma, A.H. (1962) *Sedimentology of Some Flysch Deposits: A Graphic Approach to Facies Interpretation*. Elsevier, Amsterdam, 168 pp.

Bourget, J., Zaragosi, S., Ellouz-Zimmermann, N., Ducassou, E., Prins, M.A., Garlan, T., Lanfumey, V., Rouillard, P. and **Schneider, J.-L**. Highstand vs. lowstand turbidite system growth in the Makran active margin: imprints of high-frequency external controls on sediment delivery mechanisms to deep water systems. In Press, *Accepted Manuscript, Marine Geology*.

Byrne, D.E., Sykes, L.R. and **Davis, D.M.** (1992) Great thrust earthquakes and aseismic slip along the plate boundary of the Makran subduction zone. *J. Geophys. Res.*, **97,** 449–478.

Clemens, S.C. and **Prell, W.L.** (2003) A 350,000 year summer-monsoon multi-proxy stack from the Owen Ridge, Northern Arabian Sea. *Mar. Geol.*, **201,** 35–51.

Covault, J.A., Hubbard, S.M., Graham, S.A., Hinsch, R. and **Linzer, H.-G.** (2009) Turbidite-reservoir architecture in complex foredeep-margin and wedge-top depocenters, Tertiary Molasse foreland basin system, Austria. *Mar. Petrol. Geol.*, **26,** 379–396.

Damuth, J.E. (1975) Echo-character of the western equatorial atlantic floor and its relationship to the dispersal and distribution of terrigeneous sediments. *Mar. Geol.*, **18,** 17–45.

DeMets, C., Gordon, R.G., Angus, D.F. and **Stein, S.** (1994) Effect of recent revisions to the geomagnetic reversal time scale on estimates of current plate motions. *Geophys. Res. Lett.*, **21,** 2191–2194.

Ducassou, E., Migeon, S., Mulder, T., Murat, A., Capotondi, L., Bernasconi, S.M. and **Mascle, J.** (2009) Evolution of the Nile deep-sea turbidite system during the Late Quaternary: influence of climate change on fan sedimentation. *Sedimentology*, **56,** 2061–2090.

Ellouz-Zimmermann, N., Deville, E., Muller, C., Lallemant, S.J., Subhani, A.B. and **Tabreez, A.R.** (2007a) Impact of

sedimentation on convergent margin tectonics: example of the Makran accretionary prism. In: *Thrust Belts and Foreland Basins* (Eds O. Lacombe, J. Lavé, F. Roure and J. Verges), pp. 351–366. Springer, Berlin Heidelberg.

Ellouz-Zimmermann, N., Lallemant, S., Castilla, R., Mouchot, N., Leturmy, P., Battani, A., Buret, C., Cherel, L., Desaubliaux, G., Deville, E., Ferrand, J., Lügcke, A., Mahieux, G., Mascle, G., Mühr, P., Pierson-Wickmann, A., Robion, P., Schmitz, J., Danish, M., Hasany, S., Shahzad, A. and **Tabreez, A.** (2007b) Offshore frontal part of the Makran accretionary prism: the Chamak survey (Pakistan). In: *Thrust Belts and Foreland Basins* (Eds O. Lacombe, J. Lavé, F. Roure and J. Verges), pp. 351–366. Springer, Berlin Heidelberg.

Elmore, R.D., Pilkey, O.H., Clearey, W.J. and **Curran, H.A.** (1979) The Black Shell turbidite, Hatteras Abyssal Plain, western Atlantic Ocean. *Geol. Soc. Am. Bull.*, **90,** 1165–1176.

Farre, J.A. and **Ryan, W.B.F.** (1985) 3-D view of erosional scars on U. S. mid-Atlantic continental margin. *AAPG Bull.*, **69,** 923–932.

Fleitmann, D., Burns, S.J., Mangini, A., Mudelsee, M., Kramers, J., Villa, I., Neff, U., Al-Subbary, A.A., Buettner, A., Hippler, D. and **Matter, A.** (2007) Holocene ITCZ and Indian monsoon dynamics recorded in stalagmites from Oman and Yemen (Socotra). *Quatern. Sci. Rev.*, **26,** 170–188.

Flueh, E.R., Kukowski, N. and **Reichert, C.** (1997) RV Sonne, Cruise Report SO123 'MAMUT' (Makran Murray Traverse). GEOMAR Report 62, 291 pp.

Fournier, M., Patriat, P. and **Leroy, S.** (2001) Reappraisal of the Arabia–India–Somalia triple junction kinematics. *Earth Planet. Sci. Lett.*, **189,** 103–114.

Fruehn, J., White, R.S. and **Minshull, T.A.** (1997) Internal deformation and compaction of the Makran accretionary wedge. *Terra Nova*, **9,** 101–104.

Galloway, W.E. (1998) Siliciclastic slope and base-of-slope depositional systems: Component facies, stratigraphic architecture, and classification. *AAPG Bulletin*, **82,** 569–595.

Garcia, M.H. (1993) Hydraulic, jumps in sediment-driven bottom currents. *J. Hydraul. Eng.*, **119,** 1094–1117.

Garcia, M.H. and **Parker, G.A.** (1989) Experiments on hydraulic jumps in turbidity currents near a canyon-fan transition. *Science*, **245,** 393–396.

Gardner, T.W. (1983) Experimental study of knickpoint and longitudinal profile evolution in cohesive, homogeneous material. *Geol. Soc. Am. Bull.*, **94,** 664–672.

Gasse, F. (2000) Hydrological changes in the African tropics since the Last Glacial Maximum. *Quatern. Sci. Rev.*, **19,** 189–211.

Goldfinger, C., Morey, A.E., Nelson, H., Gutierrez-Pastor, J., Johnson, J.E., Karabanov, E., Chaytor, J., Eriksson, A. and **Shipboard Scientific Party**. (2007) Rupture lengths and temporal history of significant earthquakes on the offshore and north coast segments of the Northern San Andreas Fault based on turbidite stratigraphy. *Earth Planet. Sci. Lett.*, **254,** 9–27.

Gordon, R.G. and **Demets, C.** (1989) Present-day motion along the Owen fracture zone and Dalrymple trough in the Arabian Sea. *J. Geophys. Res.*, **94,** 5560–5570.

Grando, G. and **McClay, K.** (2007) Morphotectonics domains and structural styles in the Makran accretionary prism, offshore Iran. *Sed. Geol.*, **196,** 157–179.

Gray, T.E., Alexander, J. and **Leeder, M.R.** (2005) Quantifying velocity and turbulence structure in depositing sustained turbidity currents across breaks in slope. *Sedimentology*, **52,** 467–488.

Heidarzadeh, M., Pirooz, M., Zaker, N. and **Yalciner, A.** (2009) Preliminary estimation of the tsunami hazards associated with the Makran subduction zone at the northwestern Indian Ocean. *Nat. Hazards*, **48,** 229–243.

Heiniö, P. and **Davies, R.J.** (2007) Knickpoint migration in submarine channels in response to fold growth, western Niger Delta. *Mar. Petrol. Geol.*, **24,** 434–449.

Hesse, R. and **Chough, S.K.** (1980) The Northwest Atlantic Mid-Ocean Channel of the Labrador Sea. II. Deposition of parallel laminated levee-muds from the viscous sublayer of low density turbidity currents. *Sedimentology*, **27,** 697–711.

Huyghe, P., Foata, M., Deville, E., Mascle, G. and **the Caramba Working Group.** (2004) Channel profiles through the active thrust front of the southern Barbados prism. *Geology*, **32,** 429–432.

Kenyon, N.H., Klaucke, I., Millington, J. and **Ivanov, M.K.** (2002) Sandy submarine canyon-mouth lobes on the western margin of Corsica and Sardinia, Mediterranean Sea. *Mar. Geol.*, **184,** 69–84.

Klöcker, R. and **Henrich, R.** (2006) Recent and Late Quaternary pteropod preservation on the Pakistan shelf and continental slope. *Mar. Geol.*, **231,** 103–111.

Kneller, B.C. (1995) Beyond the turbidite paradigm: physical models for deposition of turbidites and their implications for reservoir prediction. In: *Characterization of Deep Marine Clastic Systems* (Eds A.J. Hartley and D.J. Prosser), *Geol. Soc. London Spec. Publ.*, **94,** 31–49.

Kneller, B. and **Buckee, C.** (2000) The structure and fluid mechanics of turbidity currents: a review of some recent studies and their geological implications. *Sedimentology*, **47**(Suppl. 1), 62–94.

Kneller, B. and **McCaffrey, W.** (1999) Depositional effects of flow nonuniformity and stratification within turbidity currents approaching a bounding slope; deflection, reflection, and facies variation. *J. Sed. Res.*, **69,** 980–991.

Kolla, V. and **Perlmutter, M.A.** (1993) Timing of turbidite sedimentation on the Mississipi fan. *AAPG Bull.*, **77,** 1129–1141.

Komar, P.D. (1971) Hydraulic jumps in turbidity currents. *Geol. Soc. Am. Bull.*, **82,** 1477–1488.

Komar, P.D. (1973) Continuity of turbidity current flow and systematic variations in deep-sea channel morphology. *Geol. Soc. Am. Bull.*, **84,** 3329–3338.

Kubo, Y.S. and **Nakajima, T.** (2002) Laboratory experiments and numerical simulation of sediment-wave formation by turbidity currents. *Mar. Geol.*, **192,** 105–121.

Kukowski, N., Schillhorn, T., Huhn, K., von Rad, U., Husen, S. and **Flueh, E.** (2001) Morphotectonics and mechanics of the central Makran accretionary wedge off Pakistan. *Mar. Geol.*, **173,** 1–19.

Lebreiro, S.M., McCave, I.N. and **Weaver, P.P.E.** (1997) Quaternary turbidite emplacement on the Horseshoe Abyssal Plain (Iberian margin). *J. Sed. Res.*, **67,** 856–870.

Lee, S.E., Talling, P.J., Ernst, G.G.J. and **Hogg, A.J.** (2002) Occurrence and origin of submarine plunge pools at the base of the US continental slope. *Mar. Geol.*, **185,** 363–377.

Lomas, S.A. and **Joseph, P.** (2004) Confined turbidite systems. In: *Confined Turbidite Systems* (Eds S.A. Lomas and P. Joseph), *Geol. Soc. London Spec. Publ.*, **222,** 1–7.

Lowe, D.R. (1982) Sediment gravity flows. II. Depositional models with special reference to the deposits of high-density turbidity currents. *J. Sed. Petrol.*, **52,** 279–297.

Luckge, A., Doose-Rolinski, H., Khan, A.A., Schulz, H. and **von Rad, U.** (2001) Monsoonal variability in the northeastern Arabian Sea during the past 5000-years: geochemical

evidence from laminated sediments. *Palaeogeogr. Palaeoclimatol. Palaeoecol.*, **167,** 273–286.

MacDonald, R.G., Alexander, J., Bacon, J.C. and **Cooker, M.J.** (2009) Flow patterns, sedimentation and deposit architecture under a hydraulic jump on a non-eroding bed: defining hydraulic-jump unit bars. *Sedimentology*. **56,** 1346–1367.

Migeon, S., Weber, O., Faugères, J.C. and **Saint-Paul, J.** (1999) SCOPIX: a new imaging system for core analysis. *Geo-Mar. Lett.*, **18,** 251–255.

Migeon, S., Ducassou, E., Le Gonidec, Y., Rouillard, P., Mascle, J. and **Revel-Rolland, M.** (in press) Lobe construction and sand/mud segregation by turbidity currents and debris flows on the western Nile deep-sea fan (Eastern Mediterranean). *Sedimentary Geology*, doi: 10.1016/j.sedgeo.2010.02.011.

Milliman, J.D. and **Syvitski, J.P.M.** (1992) Geomorphic/tectonic control of sediment discharge to the ocean: the importance of small mountainous rivers. *J. Geol.*, **100,** 525–544.

Mitchell, N.C. (2006) Morphologies of knickpoints in submarine canyons. *Geol. Soc. Am. Bull.*, **118,** 589–606.

Mouchot, N. (2009). *Tectonique et sédimentation sur le complexe de subduction du Makran Pakistanais*. Thèse de doctorat, Université de Cergy-Pontoise, 198 pp.

Mouchot, N., Loncke, L., Mahieux, G., Bourget, J., Lallemant, S., Ellouz-Zimmermann, N. and **Leturmy, P.** (2010) Recent sedimentary processes along the Makran trench (Makran active margin, off Pakistan). *Mar. Geol.* **271,** 17–31.

Mulder, T. and **Alexander, J.** (2001) Abrupt change in slope causes variation in the deposit thickness of concentrated particle-driven density currents. *Mar. Geol.*, **175,** 221–235.

Mutti, E. and **Normark, W.R.** (1991). An integrated approach to the study of turbidite systems. In: *Seismic Facies and Sedimentary Processes of Submarine Fans and Turbidite Systems* (Eds P. Weimer and M.H. Link), pp. 75–106. Springer-Verlag, New York.

Normark, W.R., Piper, D.J.W. and **Sliter, R.** (2006) Sea-level and tectonic control of middle to late Pleistocene turbidite systems in Santa Monica Basin, offshore California. *Sedimentology*, **53,** 867–897.

Orange, D.L. (1999) Tectonics, sedimentation, and erosion in northern California: submarine geomorphology and sediment preservation potential as a result of three competing processes. *Mar Geol.*, **154,** 369–382.

Page, W.D., Alt, J.N., Cliff, L.S. and **Plafker, G.** (1979) Evidence for occurence of large magnitude earthquakes along the Makran coast of Iran and Pakistan. *Tectonophysics*, **52,** 533–547.

Payton, C.E.E. (1977). Seismic stratigraphy – application to hydrocarbon exploration. *AAPG Bull. Mem.*, **26,** 516 pp.

Pickering, K.T., Hiscott, R.N. and **Hein, F.J.** (1989) *Deep Marine Environments: Clastic Sedimentation and Tectonics* (Ed. U. Hyman), Unwin Hyman, London, 416 pp.

Piper, D.J.W. and **Deptuck, M.** (1997) Fine-grained turbidites of the Amazon Fan: facies characterization and interpretation. In: *Proceeding of the Ocean Drilling Program, Scientific Results* (Eds R.D. Flood, D.J.W. Piper, A. Klaus and L.C. Peterson), **155,** 79–108.

Piper, D.J.W. and **Normark, W.R.** (1983) Turbidite depositional patterns and flow characteristics, Navy Submarine Fan, California Borderland. *Sedimentology*, **30,** 681–694.

Piper, D.J.W. and **Normark, W.R.** (2009) Processes that initiate turbidity currents and their influence on turbidites: a marine geology perspective. *J. Sed. Res.*, **79,** 347–362.

Pirmez, C., Beaubouef, R.T., Friedmann, S.J. and **Mohrig, D.C.** (2000) Equilibrium profile and baselevel in submarine channels: examples from Late Pleistocene systems and implications for the architecture of deepwater reservoirs. *GCSSEPM Foundation 20th Annual Research Conference, Deep Water Reservoirs of the World*, pp. 782–805.

Platt, J.P., Leggett, J.K., Young, J., Raza, H. and **Alam, S.** (1985) Large-scale sediment underplating in the Makran accretionary prism, Southwest Pakistan. *Geology*, **13,** 507–511.

Posamentier, H.W. and **Weimer, P.** (1993) Siliciclastic sequence stratigraphy and petroleum geology; where to from here? *AAPG Bull.*, **77,** 731–742.

Pourmand, A., Marcantonio, F. and **Schulz, H.** (2004) Variations in productivity and eolian fluxes in the northeastern Arabian Sea during the past 110 ka. *Earth Planet. Sci. Lett.*, **221,** 39–54.

Prather, B.E. (2000) Calibration and visualization of depositional process models for above-grade slopes: a case study from the Gulf of Mexico. *Mar. Petrol. Geol.*, **17,** 619–638.

Prather, B.E. (2003) Controls on reservoir distribution, architecture and stratigraphic trapping in slope settings. *Mar. Petrol. Geol.*, **20,** 529–545.

Prather, B.E., Booth, J.R., Steffens, G.S. and **Craig, P.A.** (1998) Classification, lithologic calibration and stratigraphic succession of seismic facies of intraslope basins, Deep-Water Gulf of Mexico. *AAPG Bull.*, **82,** 701–728.

Prins, M.A. and **Postma, G.** (2000) Effects of climate, sea level, and tectonics unraveled for last deglaciation turbidite records of the Arabian Sea. *Geology*, **28,** 375–378.

Prins, M.A., Postma, G. and **Weltje, G.J.** (1999) Controls on terrigenous sediment supply to the Arabian Sea during the late Quaternary: the Makran continental slope. *Mar. Geol.*, **169,** 351–371.

von Rad, U., Schulz, H., Ali Khan, A., Ansari, M., Berner, U., Cepek, P., Cowie, G., Dietrich, P., Erlenkeuser, H., Geyh, M., Jennerjahn, T., Lückge, A., Marchig, V., Riech, V., Rösch, H., Schaëfer, P., Schulte, S., Sirocko, F., Tahir, M. and **Weiss, M.** (1995) Sampling the oxygen minimum zone off Pakistan: glacial-interglacial variations of anoxia and productivity (preliminary results, SONNE 90 cruise). *Mar. Geol.*, **125,** 7–19.

von Rad, U., Schaaf, M., Michels, K.H., Schulz, H., Berger, W.H. and **Sirocko, F.** (1999a) A 5000-yr record of climate change in varved sediments from the oxygen minimum zone off Pakistan, northeastern Arabian Sea. *Quatern. Res.*, **51,** 39–53.

von Rad, U., Schulz, H., Riech, V., den Dulk, M., Berner, U. and **Sirocko, F.** (1999b) Multiple monsoon-controlled breakdown of oxygen-minimum conditions during the past 30,000 years documented in laminated sediments off Pakistan. *Palaeogeogr. Palaeoclimatol. Palaeoecol.*, **152,** 129–161.

von Rad, U., Delisle, G. and **Luckge, A.** (2002) On the formation of laminated sediments on the continental margin off Pakistan. *Mar. Geol.*, **192,** 425–429.

Reichart, G.J., Lourens, L.J. and **Zachariasse, W.J.** (1998) Temporal variability in the northern Arabian Sea oxygen minimum zone (OMZ) during the last 225,000 years. *Paleoceanography*, **13,** 607–621.

Reichart, G.J., Schenau, S.J., de Lange, G.J. and **Zachariasse, W.J.** (2002) Synchroneity of oxygen minimum zone intensity on the Oman and Pakistan Margins at sub-Milankovitch time scales. *Mar. Geol.*, **185,** 403–415.

Ricci Lucchi, F. and **Valmori, E.** (1980) Basin-wide turbidites in a Miocene, over-supplied deep-sea plain: a geometrical analysis. *Sedimentology*, **27,** 241–270.

Rothwell, R.G., Reeder, M.S., Anastasakis, G., Stow, D.A.V., Thomson, J. and **Kahler, G.** (2000) Low sea-level stand emplacement of megaturbidites in the western and eastern Mediterranean Sea. *Sed. Geol.*, **135,** 75–88.

Sinclair, H.D. and **Tomasso, M.** (2002) Depositional evolution of confined turbidite basins. *J. Sed. Res.*, **72,** 451–456.

Sirocko, F., Sarnthein, M., Lange, H. and **Erlenkeuser, H.** (1991) Atmospheric summer circulation and coastal upwelling in the Arabian Sea during the Holocene and the last glaciation. *Quatern. Res.*, **36,** 72–93.

Sirocko, F., Garbe-Schonberg, D., McIntyre, A. and **Molęno, B.** (1996) Teleconnections between the subtropical monsoons and high-latitude climates during the last deglaciation. *Science*, **272,** 526–529.

Sirocko, F., Garbe-Schonberg, D. and **Devey, C.** (2000) Processes controlling trace element geochemistry of Arabian Sea sediments during the last 25,000 years. *Global Planet. Change*, **26,** 217–303.

Smith, R.D.A. (2004) Silled sub-basins to connected tortuous corridors: sediment distribution systems on topographically complex sub-aqueous slopes. In: *Confined Turbidite Systems* (Eds S.A. Lomas and P. Joseph), *Geol. Soc. London Spec. Publ.*, **222,** 23–43.

Snead, R.E. (1967) Recent morphological changes along the coast of West Pakistan. *Ann. Am. Assoc. Geogr.*, **57,** 550–565.

Stoffers, P. and **Ross, D.A.** (1979) Late Pleistocene and Holocene sedimentation in the Persian Gulf–Gulf of Oman. *Sed. Geol.*, **23,** 181–208.

Stow, D.A., Tabrez, A.R. and **Prins, M.A.** (2002) Quaternary sedimentation on the Makran margin: turbidity current – hemipelagic interaction in an active slope–apron system. In: *The Tectonic and Climatic Evolution of the Arabian Sea Region* (Eds P.D. Clift, D. Kroon, C. Gaedicke and J. Craig), *Geol. Soc. London Spec. Publ.*, **195,** 219–236.

Stuiver, M., Reimer, P.J. and **Reimer, R.W.** (2005) CALIB 5.0. www program and documentation.

Talling, P.J., Amy, L.A. and **Wynn, R.B.** (2007) New insights into the evolution of large-volume turbidity currents: comparison of turbidite shape and previous modelling results. *Sedimentology*, **54,** 737–769.

Toniolo, H. and **Cantelli, A.** (2007) Experiments on upstream-migrating submarine knickpoints. *J. Sed. Res.*, **77,** 772–783.

Tripsanas, E.K., Bryant, W.R. and **Phaneuf, B.A.** (2004) Depositional processes of uniform mud deposits (unifites), Hedberg Basin, northwest Gulf of Mexico: new perspectives. *AAPG Bull.*, **88,** 825–840.

Underwood, M.B. and **Karig, D.E.** (1980) Role of submarine canyons in trench and trench slope sedimentation. *Geology*, **8,** 432–436.

Unterseh, S. (1999) *Cartographie et Caractérisation du Fond Marin par Sondeur Maultifaisceaux*. Thèse de 3eme cycle, Institut National Polytechnique de Lorraine, 234 pp.

Waltham, D. (2004) Flow transformations in particulate gravity currents. *J. Sed. Res.*, **74,** 129–134.

Weyhenmeyer, C.E., Burns, S.J., Waber, H.N., Aeschbach-Hertig, W., Kipfer, R., Loosli, H.H. and **Matter, A.** (2000) Cool glacial temperatures and changes in moisture source recorded in Oman groundwaters. *Science*, **287,** 842–845.

White, R.S. and **Louden, K.E.** (1983) The Makran continental margin: structure of a thickly sedimented convergent plate boundary. In: *Studies in Continental Margin Geology* (Eds J.S. Watkins and C.L. Drake), *Mem. Am. Assoc. Petrol. Geol.*, **34,** 499–518.

Wynn, R.B., Weaver, P.P.E., Masson, D.G. and **Stow, D.A.V.** (2002) Turbidite depositional architecture across three interconnected deep-water basins on the north-west African margin. *Sedimentology*, **49,** 669–695.

Zaragosi, S., Bourillet, J.-F., Eynaud, F., Toucanne, S., Denhard, B., Van Toer, A. and **Lanfumey, V.** (2006) The impact of the last European deglaciation on the deep-sea turbidite systems of the Celtic-Armorican margin (Bay of Biscay). *Geo-Mar. Lett.*, **26,** 317–329.

Manuscript received 21 July 2009; revision accepted 17 March 2010